Celest Mech Dyn Astr (2015) 122:263–302
DOI 10.1007/s10569-015-9619-2

ORIGINAL ARTICLE

Natural motion around the Martian moon Phobos: the dynamical substitutes of the Libration Point Orbits in an elliptic three-body problem with gravity harmonics

M. Zamaro[1] · **J. D. Biggs**[1]

Received: 22 December 2014 / Revised: 7 March 2015 / Accepted: 18 April 2015 /
Published online: 10 May 2015

Abstract The Martian moon Phobos is becoming an appealing destination for future scientific missions. The orbital dynamics around this planetary satellite is particularly complex due to the unique combination of both small mass-ratio and length-scale of the Mars–Phobos couple: the resulting sphere of influence of the moon is very close to its surface, therefore both the classical two-body problem and circular restricted three-body problem (CR3BP) do not provide an accurate approximation to describe the spacecraft's dynamics in the vicinity of Phobos. The aim of this paper is to extend the model of the CR3BP to consider the orbital eccentricity and the highly-inhomogeneous gravity field of Phobos, by incorporating the gravity harmonics series expansion into an elliptic R3BP, named ER3BP-GH. Following this, the dynamical substitutes of the Libration Point Orbits (LPOs) are computed in this more realistic model of the relative dynamics around Phobos, combining methodologies from dynamical systems theory and numerical continuation techniques. Results obtained show that the structure of the periodic and quasi-periodic LPOs differs substantially from the classical case without harmonics. Several potential applications of these natural orbits are presented to enable unique low-cost operations in the proximity of Phobos, such as close-range observation, communication, and passive radiation shielding for human spaceflight. Furthermore, their invariant manifolds are demonstrated to provide high-performance natural landing and take-off pathways to and from Phobos' surface, and transfers from and to Martian orbits. These orbits could be exploited in upcoming and future space missions targeting the exploration of this Martian moon.

Keywords Phobos · Libration Point Orbits · Gravity harmonics · Invariant manifolds · Dynamical systems theory · Numerical continuation · Phobos surface

✉ M. Zamaro
mattia.zamaro@strath.ac.uk

J. D. Biggs
james.biggs@strath.ac.uk

[1] Advanced Space Concepts Laboratory, University of Strathclyde, 75 Montrose Street, Glasgow G1 1XJ, UK

1 Introduction

One of the most famous and historically investigated chaotic dynamical systems is the circular restricted problem of three bodies (CR3BP), which models the motion of a point-mass subject to the gravitational field generated by two spherical homogeneous bodies moving in circular orbits around their common center of mass. In the past few decades, dynamical systems tools developed for this problem have provided an in-depth understanding of the spacecraft's natural dynamics (Koon et al. 2011). The orbits around the Libration points (LPOs) have been computed extensively, using semi-analytical methods [such as Lindstedt–Poincaré series expansions (Koon et al. 2011; Masdemont 2004)] and numerical techniques [such as numerical continuation (Koon et al. 2011; Gómez and Mondelo 2001)], for the Sun–Earth and Earth–Moon systems, where the approximation of the natural dynamics using the CR3BP is an accurate one (Farquhar 1968; Howell 1984; Conley 1969; McGehee 1969; Koon et al. 2000). The study of the invariant motions of these systems has proved invaluable for real space missions, such as ISEE-3/ICE (1978), WIND (1994), SOHO (1995), ACE (1997) and Genesis (2001), where they have been exploited as energy-efficient trajectories to minimize the spacecraft's fuel consumption during station-keeping and orbital transfers.

However, future space missions are now targeting deep space celestial bodies, such as asteroids and planetary satellites. In particular, the two moons of Mars, Phobos and Deimos, have been proposed as attractive destinations since the early 80s (Singer 1981; O'Leary 1985). Scientific interest in these moons focuses on understanding their composition and enigmatic origin, which would provide insight into the Solar System's origin itself. The American Viking program (1975) and Soviet Phobos-2 spacecraft (1988) were the first missions to successfully provide images of the two moons. Using this information, the modeling of their shape and gravity field became an extensive area of research (Turner 1978; Chao and Rubincam 1989) which continues today (Willner 2009). In addition, the Martian moons' exploration has been highlighted as a key milestone to the long term goal of a human mission to Mars (Sommerer 2014; Hopkins and Pratt 2011; Lee 2012). In particular Phobos, the innermost and larger moon of the two, is considered to be an ideal candidate for landing a spacecraft as a precursor to a landing mission on Mars (Brandenburg 2012; Troutman 2014; Price et al. 2014). Past missions designed to land on Phobos have all failed (Phobos-1 and Phobos-2, Phobos-Grunt). Currently, ESA is scheduling a sample-and-return mission to Phobos (McCaughrean 2012; Koschny 2012) and NASA is targeting this moon to test a new kind of rover for planetary exploration (Pandika 2012; Dorminey 2013).

This growing interest in undertaking a successful mission have fostered in recent years the need to probe suitable orbits around Phobos. Early analysis focused on simple hovering station-keeping (Bombardelli 2012) and exploitation of stable Quasi-Satellite orbits (Gil and Schwartz 2010; da Silva Pais Cabral 2011; Lidov and Vashkov'yak 1993). The latter are orbits around Mars where the spacecraft flies in close co-orbital configuration with Phobos, and have been applied in the design of past missions. In contrast, the LPOs have not received a lot of attention because the orbital dynamics of the CR3BP, where the two primaries are Mars and Phobos, do not provide a suitable approximation of the natural dynamics in the vicinity of the moon, where many strong perturbations are involved. In Wallace et al. (2012) a multiple shooting method is used in a high-fidelity perturbation model to correct the classical LPOs of the Mars–Phobos CR3BP. The resulting solutions are only bounded for a specific time span and do not contain any information on the natural frequencies of the perturbations, and are therefore not appropriate dynamical substitutes (Gómez et al. 2002) nor their performance analysis suitable to be optimized in the mission design loop.

The aim of this paper is to extend the model of the CR3BP to describe the accurate dynamics of a spacecraft in the vicinity of Mars' moon Phobos, and derive the dynamical substitutes of the LPOs in this new system. Phobos has a highly inhomogeneous gravity field and the eccentricity of its orbit around Mars has a significant effect in designing orbits in its proximity. The inclusion of the eccentricity in the well-known elliptic R3BP (ER3BP) (Szebehely 1967) often uses a rotating-pulsating frame to maintain a natural similarity with the CR3BP, which is particularly suitable for performing numerical continuation with respect to the eccentricity parameter to obtain the corresponding dynamical substitutes of Libration points and LPOs (Szebehely 1967; Broucke 1969). In the last two decades, the orbital dynamics around highly irregular shaped bodies have been investigated using tetrahedrons to model their surface (Werner 1994), and applied in the framework of a perturbed 2B dynamics to derive equilibrium points and orbits around them in proximity of asteroids (Yu and Baoyin 2012a, b). These orbits are defined in the asteroid's body-fixed frame and are not significantly influenced by the Sun's third-body perturbation (Yu and Baoyin 2012b; Ni et al. 2014). The manifold of the LPOs is instead defined in the Sun-asteroid orbital frame and far from the asteroid, and is not significantly influenced by the irregularities of its gravity field (Abouelmagd and Sharaf 2013). The two dynamical domains are therefore decoupled in the phase-space of the asteroids' orbital dynamics. On the contrary, the relative dynamics around a small planetary satellite like Phobos cannot neglect any of these forces.

The outline of the paper is as follows. In Sect. 2 we derive a new model extending the classical CR3BP to an ER3BP with an inhomogeneous gravity field of the second massive body, described through a gravity harmonics series expansion (ER3BP-GH). Subsequently in Sect. 3, we present the procedures of dynamical systems theory that use the LPOs in the CR3BP as an initial guess in numerical continuation schemes (Keller 1977; Allgower and Georg 2003), that allow us to compute their dynamical substitutes (Gómez et al. 2002) in the new, more realistic, model. Section 4 presents the resulting periodic and quasi-periodic LPOs in the Mars–Phobos ER3BP-GH. In Sect. 5, the related applications and performances are presented, for example their lighting conditions, surface coverage and passive radiation shielding. Furthermore, the invariant manifolds (IMs) of the LPOs in this more realistic dynamical model are computed, and due to the proximity of the moon, they are demonstrated as natural landing and take-off gateways to and from its surface. In particular, we identify natural trajectories that provide the lowest angle of incidence and escape velocity to and from their arrival and departure sites respectively. Section 6 concludes the paper and suggests potential applications for these orbits and their IMs in future space missions to Phobos. In addition, we propose that these trajectories can help to explain the formation of the craters and grooves of the moon, as well as the dust dynamics around it, and the new model with gravity harmonics can provide further evidence to support the theory of accretion for the origin of Phobos.

2 Modeling of the relative orbital dynamics around Phobos

This section focuses on the derivation of an appropriate model to approximate the orbital dynamics of a spacecraft in the proximity of Phobos, tailored to be used for the computation of the Libration Point Orbits (LPOs) in Sect. 3. Table 1 presents a summary of the physical and orbital parameters of Mars and Phobos that have been used in the analysis undertaken in this paper. The standout characteristics of Phobos are its small size (even smaller than some asteroids) and its irregular shape, as represented in Fig. 1. Phobos moves in a relatively low

Table 1 Physical and astrodynamical properties

Property	Mars	Phobos
m (kg)	6.42×10^{23}	1.07×10^{16}
Size (km)	R mean sphere	R mean ellipsoid
	3.39×10^{3}	$13.1 \times 11.1 \times 9.30$
Revolution T	687 days	7.65 h
Rotation T	24.6 h	7.65 h
θ (°)	25.2	0.301
Gravity field	*GHs*	*GHs*
J_2	0.00196	0.105
$J_{2,2}$	0.0000631	0.0147
J_3	0.0000315	0.00775
J_4	0.0000154	0.0229
Orbital elements	Sun-Ecliptic	Mars-Equatorial
a (km)	2.28×10^{8}	9.38×10^{3}
e	0.0934	0.0156
i (°)	1.85	1.07

All the values are rounded to 3 digits. Full values up to 16 digits are used in this paper, and are retrieved from the following sources. Ephemerides: NASA JPL at 25th July 2012 00.00CT. Phobos axial tilt θ at date: mean value at epoch 1.08°. Gravity models: Mars MGM1025, Phobos (Chao and Rubincam 1989)

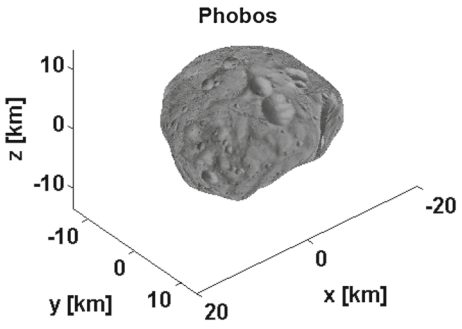

Fig. 1 Phobos. Shape harmonics model (Willner 2009), Hill's frame. Stickney is the large crater on the *right side*

altitude and almost circular and equatorial orbit around Mars, and it rotates with synchronous period and almost zero-tilt with respect to its orbital motion.

Let's now define two reference frames in Cartesian coordinates that will be used extensively in this paper.

- Phobos' Hill's frame has its origin in the moon's barycenter and rotates with fixed attitude with respect to its orbit around Mars, with vertical z-axis perpendicular to the orbital plane, and radial x-axis pointing outwards from the Mars–Phobos barycenter.
- Phobos' body-centered body-fixed frame (BCBF) has its origin in the moon's barycenter and its attitude is fixed with respect to the moon's geometry, with vertical z-axis aligned along the body's spin axis, and x-axis pointing towards the body's Prime Meridian intersection on the equatorial plane.

The fact that not only the revolution of Phobos around Mars and the rotation around its spin axis are synchronous, but that they are also respectively equatorial and zero-tilted (Duxbury and Callahan 1981), implies that Phobos' attitude, expressed by the body's BCBF frame, is approximately fixed in the orbital Hill's frame. With this approximation, their respective z-axes are coincident, while their x-axes differ only by the definition of the Prime Meridian.

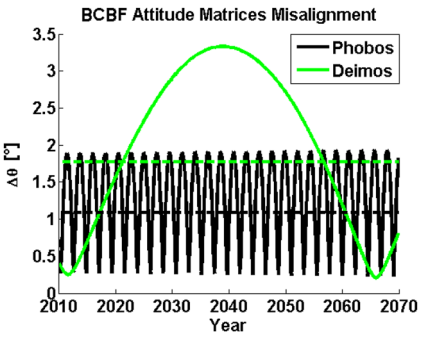

Fig. 2 Misalignment angle between the equatorial and orbital planes of the Martian moons. Mean values in *dotted lines*

In particular, Phobos' Prime Meridian is formally identified by the location of the point constantly pointing towards Mars on the body's Equator (Archinal et al. 2010; Duxbury and Callahan 1981). Therefore the two frames differ by a rotation of 180° of their x-y plane's axes. Before the definition of the Prime Meridian, the actual misalignment between the two frames oscillates between a minimum of 0.30° and a maximum of 1.90°, and the dynamics of this libration motion is much slower than the time-scale of a mission segment around Phobos (period of 2.26 terrestrial years), as presented in Fig. 2. In this paper, we approximate the two frame's attitudes to be fixed and with zero-tilt with respect to each other. It is also interesting to recall that such nominal configuration corresponds to the stable orientation provided by the central body's gravity-gradient torque: Phobos' Hill's and BCBF frames' axes correspond to the body's principal axes of inertia.

2.1 The Mars–Phobos CR3BP

The study of the Mars–Phobos-spacecraft system is conducted in the first instance with the CR3BP model (Koon et al. 2011), which is to consider the gravitational effect of the spacecraft negligible with respect to the two massive bodies (1: Mars; 2: Phobos) moving in a Keplerian circular orbit. The dynamics of the CR3BP is expressed in a third rotating reference frame.

– The 3B frame corresponds to Phobos' Hill's frame except for the origin, which is the Mars–Phobos system's barycenter.

The CR3BP is expressed in non-dimensional units, setting the unit of mass to be the total mass of the system, and the unit of length L to be the semi-major axis of the orbit of the two primaries. In addition the time is set to correspond to the mean anomaly of their orbit. The only parameter of the normalized time-invariant CR3BP is the mass ratio μ, the normalized mass of the second body, which for the case of the Mars–Phobos couple is

$$\mu = 1.66059511088139 \times 10^{-8}$$

Note that the mass parameter of the system is very small, if compared to other cases of Sun-planet or planet–satellite couples of primaries studied in the Solar System. In contrast the mass parameter of a Sun-asteroid R3BP is far lower than our μ. In addition, the length unit of the system is very small too since the altitude of Phobos' orbit is less than twice the radius R_1 of Mars

$$R_1/L = 36\,\%$$

This is an uncommon condition for all the general pairs of primaries of the Solar System.

The equations of motion of the CR3BP are stated in Eq. (1), where $\mathbf{q} = [x; y; z]$ is the position of the spacecraft in the normalized 3B frame, and $\mathbf{x} = [\mathbf{q}; \dot{\mathbf{q}}]$[1] is the resulting state of the vectorfield $\mathbf{f}$ of the dynamical system reduced to first order. Such general notation will be maintained throughout this paper, where the position will refer to the frame of the current model, which is identified by the vectorfield's subscript. We also use the common expressions $\mathbf{I_n}$, $\mathbf{0_n}$, $\mathbf{0_{nxm}}$ to indicate respectively an identity, square and rectangular null matrix of dimensions n and m. In Eq. (1), $u(\mathbf{q}) = u_{G_1}(\mathbf{q}) + u_{G_2}(\mathbf{q})$ is the gravitational potential of the two massive bodies (only a function of $\mathbf{q}$): in the CR3BP they are considered spherical and homogeneous, therefore each term is $u_{G_\oplus} = Gm_\oplus/||\mathbf{q} - \mathbf{q}_\oplus||$, where G is the gravitational constant, $m_\oplus$ and $\mathbf{q}_\oplus$ are the mass and position of the body $\oplus$ in the 3B frame, and are expressed in normalized units. The resulting gravity acceleration is the Cartesian gradient $\nabla = \left[\frac{\partial}{\partial x}; \frac{\partial}{\partial y}; \frac{\partial}{\partial z}\right]$ of the potential. In particular, the gravity of both bodies is time-invariant because in this rotating reference frame their positions are fixed along the x-axis ($x_1 = -\mu, x_2 = 1 - \mu$ in L units). Since the normalized angular velocity of the 3B frame is $\omega = \hat{\mathbf{z}} = [0; 0; 1]$, the notation is simplified by defining the skew-symmetric matrix $\mathbf{W} \in \mathbb{R}^{3\times3}$: $\mathbf{W} \cdot (\cdot) = \hat{\mathbf{z}} \wedge (\cdot)$ and the related matrix $\mathbf{P} = \mathbf{W}^2$, to yield the CR3BP in the system of first-order ordinary differential equations (ODEs).

$$\dot{\mathbf{x}} = \mathbf{f_{CR3BP}}(\mathbf{x}) = \begin{bmatrix} \mathbf{0_3} & \mathbf{I_3} \\ -\mathbf{P} & -2\mathbf{W} \end{bmatrix} \mathbf{x} + \begin{bmatrix} \mathbf{0_{3x1}} \\ \nabla u(\mathbf{q}) \end{bmatrix} \tag{1}$$

The solution at time t is provided by the flow map $\phi_{\mathbf{f}}(t, t_0, \mathbf{x}_0) = \mathbf{x}(t)$, which depends from the initial condition $\mathbf{x}_0$ at t_0. The CR3BP defined above is a non-integrable time-invariant Hamiltonian system, whose integral of motion is usually called the Jacobi integral c, which can be related to the mechanical energy per unit of mass ϵ of the system. In relative dynamics, the effective potential u_{eff} is usually introduced to resemble the two classical components of the mechanical energy.

$$c(\mathbf{x}) = -\dot{\mathbf{q}}^T\dot{\mathbf{q}} + \mathbf{q}^T\mathbf{q} + 2u(\mathbf{q}) = -\dot{\mathbf{q}}^T\dot{\mathbf{q}} + 2u_{eff}(\mathbf{q}) = -2\varepsilon(\mathbf{x}) \tag{2}$$

The Hill's surfaces, or zero-velocity surfaces, are the iso-surfaces in the position domain of the Jacobi integral with null velocity. For a given initial condition $\mathbf{x}_0$, the related Hill's surface defines the boundary of the 3D position-space where the natural motion is constrained. In particular, the Hill's sphere of influence (SOI) is the region around each body where the dynamics is dominated by its own gravity field: placing a point at zero relative velocity inside the SOI would result in an attraction towards the respective body. In the framework of the CR3BP, the second primary's SOI normalized radius is defined as $\sqrt[3]{\mu/3}$ (Koon et al. 2011). For Phobos, this radius is 0.17 % of the distance from Mars, which is an altitude over the moon's mean sphere of only 5.5 km. This means that the physical space that can be used to orbit around Phobos is very close to the body at low energy, and considering the fact that Phobos is very irregular in its shape, the maximum altitude of the Hill's SOI boundary is of only 3.5 km, as shown in Fig. 3 (left) using the moon's mean ellipsoid. Therefore it is impossible to naturally orbit around Phobos with a Keplerian motion.

As μ and L decrease in the CR3BP, the SOI shrinks close to the surface of the secondary body. Thus, the two peculiarities of the Mars–Phobos couple previously highlighted are responsible for the reduction of the exploitable realm of attraction of the moon. This result significantly affects the LPOs of the three-body dynamics, and will be referred throughout this paper as the collapsing effect of the SOI. In particular an analysis of the physical and orbital characteristics for all the major couples of primaries of the Solar System was undertaken

[1] The dot over a variable represents the time-derivative operator.

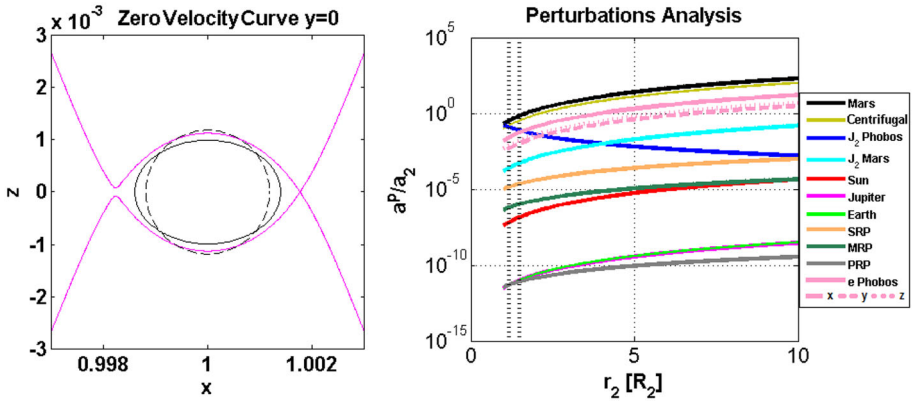

Fig. 3 *Left* Hill's surface for L_2 energy. x–z projection. Phobos mean sphere (*dashed line*) and ellipsoid (*plain line*). Axes normalized in L units. *Right* Differential perturbations analysis. *Vertical dotted lines* indicate Phobos major size and Hill's SOI radius. Distance from Phobos in mean radii

by computing the related Hill's SOI radius. We considered two maximum thresholds for the altitude of the Hill's SOI over the secondary's mean radius: 10 km for practical mission operation constraints, and 1 radius to define an outer boundary such that, within this altitude, perturbations due to the secondary body significantly influence the motion. Within these two absolute and relative thresholds, in addition to Mars–Phobos, only five other couples of primaries fall inside, and therefore are characterized by the same collapsing effect. They are all cases of planetary satellites: three moons of Saturn (Pan, Daphnis, Atlas), one of Uranus (Cordelia), and one of Neptune (Naiad), while four inner moons of Jupiter have their Hill's SOI inside their body. Orbital dynamics in proximity of these bodies are therefore very complex: no Keplerian solutions (where the central body is the secondary) nor classical LPOs of the CR3BP exist because the natural motion is highly influenced by the perturbations of the secondary body, since these moons are all highly inhomogeneous. However, as the contraction of the SOI indirectly drags the manifold of distant orbits (where the central body is the primary) closer to the secondary, the Quasi-Satellite orbits (Gil and Schwartz 2010) are also much closer than in classical systems studied with a CR3BP. It is worth noting that despite the small μ yielding a small normalized radius of the SOI, the collapsing effect is not encountered in the case of a Sun-asteroid couple because L is too large. For example, considering a distance of 1AU, even with a hypothetical small bulk density of 1000 kg/m^3, the relative altitude of the SOI of a body orbiting around the Sun is more than 100 times its mean sphere's radius.

2.2 Orbital perturbations

An analysis is undertaken to quantify approximately the errors that occur in the Mars–Phobos system when it is approximated with a CR3BP. The first orbital perturbation is due to the non-spherical gravity of both Mars and Phobos, where the dominant term is known as J_2 and is related to the body's oblateness, and has been evaluated including also its apparent acceleration acting on the 3B frame. The second source of gravitational perturbation is the effect of additional bodies, considered in their closest conjunction configuration with Phobos, that in the framework of the 3BP is referred as a fourth body perturbation. Furthermore, the radiation pressures of the Sun (SRP), Mars (MRP, enclosing also the portion of the albedo

of the SRP), and Phobos (PRP, with its albedo) are computed. In addition to these physical forces, the modeling perturbations represented by the approximation of the dynamics as a circular R3BP are taken into account, which is the effect of the eccentricity of the Mars–Phobos orbit. To derive a related physical acceleration value, we consider the difference between the acceleration field of the CR3BP and the one of the elliptic model of the Mars–Phobos system, and take the maximum over the orbital phases of Phobos, with the reference of the same relative state with respect to Phobos.

An important point to consider is that Phobos' orbit around Mars is not Keplerian, but more closely follows a classical low-altitude J_2 perturbed orbit. Therefore, the analysis of every orbital perturbation which is not due to Phobos (gravity and PRP) in its proximity must be conducted in the framework of the relative dynamics with respect to Phobos, considering the resulting differential perturbation.

Since this analysis is undertaken to derive a basic reference for the orbital perturbations, it will be applied for the simple case of fixed relative points. Also, as we are interested in the dynamics near Phobos, due to the small size of its SOI, all the perturbations are nearly isotropic, and the only variable for this simple analysis is the radial distance from Phobos along the Mars–Phobos direction (apart from the eccentricity, which has been evaluated along all three directions). Outcomes of the differential analysis are presented in Fig. 3 (right), where the magnitude of the perturbations a^P is shown as a ratio a^P/a_2 with respect to the magnitude a_2 of Phobos' Keplerian gravity term at the point, and they correspond to Gil (2007). In conclusion, the CR3BP does not provide an accurate approximation to describe the Mars–Phobos system's dynamics: the gravity harmonics and the orbital eccentricity of Phobos are the main orbital perturbations in proximity of the moon. Outside its Hill's SOI boundary the eccentricity becomes the dominant term, with Mars J_2 the second most influential. In this paper both the gravity harmonics and eccentricity are incorporated into the modeling of the relative dynamics near Phobos, as will be described in Sects. 2.3 and 2.4.

2.3 The Mars–Phobos CR3BP-GH

The modeling of the external gravity field of convex bodies is provided by a spherical harmonics series expansion, known as gravity harmonics (GHs). Usually complex shaped asteroids require an appropriate discrete distribution of tetrahedrons to model their surface and derive the related gravity field, because both the shape and the field cannot be described by a single-valued function in the spherical coordinates of the body's BCBF frame (Willner 2009). However, in the case of Phobos the GHs have proved suitable to model its gravity field. From a previous paper (Chao and Rubincam 1989) which collates the data obtained through Viking observations, we are provided with a model of Phobos' gravity field: the related GHs are stated up to degree and order 4, with the most important terms summarized in Table 1. In Werner (1994), the tetrahedron approach was applied to Phobos and results compared with a GHs series expansion that is based on the same Viking's data and is stated up to degree and order 6 (Martinec et al. 1989): the conclusion made by the author was that the two techniques produce similar results. Therefore, the GHs technique was used to model the gravity field of Phobos in this paper. The advantage is that the GHs are analytical functions, with far less computational cost than using a mesh of tetrahedrons, and the accuracy of the approximation could be naturally tuned by the terms of the series to be considered, unlike the tetrahedron method. We also chose to use the lower order GHs model of Chao and Rubincam (1989), and use the model of Martinec et al. (1989) as a more accurate benchmark reference: the error between the two gravity fields at the SOI's boundary is of the order of a few percent of the

cumulated GHs perturbation at this distance. The methodology developed in this paper will not change, and the outcomes will just depend on the series' coefficients.

The key point is that Phobos' BCBF frame, where the GHs are defined, is aligned with the 3B frame, therefore the equations of motion of the Mars–Phobos CR3BP with Phobos' GHs (named CR3BP-GH) remain time-invariant in the classical 3B frame. The actual misalignment was presented in Fig. 2, and is evaluated in the following way. Consider the four angles $\Omega_{\oplus}$, $i_{\oplus}$, $\omega_{\oplus}$, $\nu_{\oplus,0}$ of the Keplerian orbital elements of the body $\oplus$, and $n_{REV_{\oplus}}$, $n_{ROT_{\oplus}}$ are its revolution and rotational spin rates. The orbital elements of Phobos are defined in a frame centered in Mars, with the z-axis aligned along Mars' spin axis, and the x-axis pointing towards the Mars' Node of reference Ω_{N_1} (Archinal et al. 2010). The BCBF frame of a body $\oplus$ is expressed by the right ascension $\alpha_{NP_{\oplus}}$ and declination $\delta_{NP_{\oplus}}$ of its North Pole: these physical characteristics are defined in the J2000 frame for every Solar System's planet or satellite (Archinal et al. 2010). They define the North Pole's inclination $i_{NP_{\oplus}} = \frac{\pi}{2} - \delta_{NP_{\oplus}}$, and the Node of reference's location $\Omega_{N_{\oplus}} = \frac{\pi}{2} + \alpha_{NP_{\oplus}}$. Finally, the initial location of the body's Prime Meridian from its Node of reference is given by $\Omega^{N_{\oplus}}_{PM_{\oplus},0}$. Let $\mathbf{A}^{F1}_{F2}$ define the attitude matrix that rotates a vector's components from the frame $F1$ to the frame $F2$. The sought $\mathbf{A}^{BCBF}_{3B}$ is given by a succession of elementary rotations, where the attitude matrix $\mathbf{A_n}(\alpha)$ represents a rotation of α around the axis $n = 1, 2, 3$ of the current frame (x, y, z) of basis $(\hat{\mathbf{e}}_1, \hat{\mathbf{e}}_2, \hat{\mathbf{e}}_3)$.

$$\begin{aligned}\mathbf{A}^{BCBF}_{3B} = {} & \mathbf{A_3}\left(n_{REV_2}t + \nu_{2,0} + \omega_2\right)\mathbf{A_1}\left(i_2\right)\mathbf{A_3}\left(\Omega_2\right)\mathbf{A_1}\left(i_{NP_1}\right)\cdot \\ & \mathbf{A_3}\left(\Omega_{N_1} - \Omega_{N_2}\right)\mathbf{A_1}\left(-i_{NP_2}\right)\mathbf{A_3}\left(-\Omega^{N_2}_{PM_2,0} - n_{ROT_2}t\right)\end{aligned} \tag{3}$$

This matrix is generally a function of the time t. The time-dependency is erased if and only if the rotation and revolution are synchronous, and the cluster of the five central matrices of Eq. (3) is reduced to a single matrix $\mathbf{A_3}(\Omega_2 - \Omega_{N_2})$. This central core of Eq. (3) represents the attitude matrix between the orbital and equatorial frames of the second body. The first condition $n_{REV_2} = n_{ROT_2}$ is true for Phobos, while the misalignment between Phobos' orbital and equatorial planes of the second condition is evaluated with the real ephemerides along time of Phobos (Duxbury and Callahan 1981): the related Euler angle represents the tilt angle shown in Fig. 2. Since this angle is relatively small (maximum 1.90°) it is approximated to be null, and the attitude matrix between the two frames becomes:

$$\mathbf{A}^{BCBF}_{3B} = \mathbf{A_3}(-\Omega^{R^1_2}_{PM_2}) = \mathbf{A_3}(-\pi) \tag{4}$$

where the location $\Omega^{R^1_2}_{PM_2}$ of Phobos' Prime Meridian (x-axis of BCBF) with respect to the Mars–Phobos radial (x-axis of 3B) is constant and formally set to $180° = \pi$ rad as explained at the beginning of Sect. 2. This approximation could be estimated to produce a residual orbital perturbation on the new CR3BP-GH of two orders of magnitude lower than the one provided by the cumulated GHs perturbation on the CR3BP. This, together with the inaccuracy of the GHs' coefficients, is a first estimation of the savings that will be provided by tracking the orbits computed in a more accurate description of the natural dynamics.

The gravitational potential $u_{G_{\oplus}}$ described by the series expansion of spherical harmonics is presented in Eq. (5) (Kaula 1966), where $R_{\oplus}$ is a reference radius, in our case the equivalent-volume radius of the body $\oplus$. It is still a function of the position in the 3B frame, but the series expansion of GHs is expressed in term of its spherical coordinates in the BCBF frame: $\mathbf{q}_{BCBF} = (\mathbf{A}^{BCBF}_{3B})^T(\mathbf{q} - \mathbf{q}_{\oplus})$. The transformation from Cartesian to spherical coordinates $[r; \vartheta; \psi] = \mathbf{T}_{TSE}([x; y; z])$ is described by magnitude r, co-latitude ϑ from the body's

North Pole, East-longitude ψ with respect to the body's Prime Meridian, and the related physical basis $(\hat{\mathbf{e}}_r,\ \hat{\mathbf{e}}_\vartheta,\ \hat{\mathbf{e}}_\psi)$ defines the local TSE frame.

$$\begin{cases} u_{G_\oplus}(\mathbf{q}) = u_{G_\oplus}(r,\vartheta,\psi) = \frac{Gm_\oplus}{R_\oplus}\sum_{n=0}^{\infty}\left(\frac{R_\oplus}{r}\right)^{n+1}\sum_{m=0}^{n} C_n^m(\psi)\,P_n^m(\cos\vartheta) \\ C_n^m(\psi) = C_{n,m}\cos m\psi + S_{n,m}\sin m\psi = J_{n,m}\cos m\left(\psi-\lambda_{n,m}\right) \end{cases} \tag{5}$$

The double expansion is conducted with degree n and order m, using the Legendre associated polynomials P_n^m, functions of the co-latitude, which are scaled with two n,m-dependent coefficients linearly combined with harmonic functions of the longitude: C and S (or related magnitude J and phase λ) are the Stokes coefficients pair for each degree and order of the series expansion. The series are truncated at the maximum degree and order of the GHs coefficients. The first term $J_{0,0} = 1$ provides the basic spherical term used in Sect. 2.1 in the CR3BP, therefore all the other terms constitute the perturbation of the GHs. A similar series expansion is available for describing the real shape of Phobos (Willner 2009), which is expressed up to degree and order 17. The related shape harmonics will be used from now on to model the surface of Phobos for practical applications, as represented in Fig. 1.

From the definition of the potential, the gravitational acceleration of Phobos is obtained through the spherical gradient $\nabla_{TSE} = \left[\frac{\partial}{\partial r};\ \frac{1}{r}\frac{\partial}{\partial\vartheta};\ \frac{1}{r\sin\vartheta}\frac{\partial}{\partial\psi}\right]$, then rotated in the BCBF frame through the local attitude matrix of Eq. (6), where ϕ is the latitude.

$$\mathbf{A}_{TSE}^{BCBF}(\mathbf{q}) = \mathbf{A}_{TSE}^{BCBF}(\phi,\psi) = \mathbf{A}_1\left(-\frac{\pi}{2}\right)\mathbf{A}_2(-\phi)\,\mathbf{A}_3(\psi) = \mathbf{A}_3(-\phi)\,\mathbf{A}_1\left(-\frac{\pi}{2}\right)\mathbf{A}_3(\psi) \tag{6}$$

For the following applications that will be presented in Sect. 3, the Hessian matrix of the potential is required, and it is obtained through the spherical Hessian $\mathbf{H}_{TSE}$, then rotated and counter-rotated through $\mathbf{A}_{TSE}^{BCBF}$. The Hessian in spherical coordinates is computed from the Hessian definition for a general curvilinear coordinates basis, that makes use of the metric matrix $\boldsymbol{g}$ and the Christoffels' symbols Γ of the coordinate transformation (Brannon 2004), in our case $\mathbf{T}_{TSE}$, and is presented in Eq. (7).

$$\mathbf{H}_{TSE} = \begin{bmatrix} \frac{\partial^2}{\partial r^2} & \frac{\partial}{\partial r}\left(\frac{1}{r}\frac{\partial}{\partial\vartheta}\right) & \frac{\partial}{\partial r}\left(\frac{1}{r\sin\vartheta}\frac{\partial}{\partial\psi}\right) \\ \frac{\partial}{\partial r}\left(\frac{1}{r}\frac{\partial}{\partial\vartheta}\right) & \frac{1}{r^2}\frac{\partial^2}{\partial\vartheta^2}+\frac{1}{r}\frac{\partial}{\partial r} & \frac{1}{r}\frac{\partial}{\partial\vartheta}\left(\frac{1}{r\sin\vartheta}\frac{\partial}{\partial\psi}\right) \\ \frac{\partial}{\partial r}\left(\frac{1}{r\sin\vartheta}\frac{\partial}{\partial\psi}\right) & \frac{1}{r}\frac{\partial}{\partial\vartheta}\left(\frac{1}{r\sin\vartheta}\frac{\partial}{\partial\psi}\right) & \frac{1}{r^2\sin^2\vartheta}\frac{\partial^2}{\partial\psi^2}+\frac{1}{r}\frac{\partial}{\partial r}+\frac{\cos\vartheta}{r^2\sin\vartheta}\frac{\partial}{\partial\vartheta} \end{bmatrix} \tag{7}$$

The gravitational potential of Phobos is extended in the GHs series expansion: $J_{0,0} = 1$, degree-1 terms are null for barycentric frames, therefore the net gravitational perturbation of Phobos $\mathbf{a}_{\mathbf{G_2}}^{\mathbf{p}}$, starting from $J_{2,0} = 0.105$, is added to the CR3BP vectorfield to derive the equations of motion of the CR3BP-GH in the classical 3B frame.

$$\dot{\mathbf{x}} = \mathbf{f}_{\mathbf{CR3BPGH}}(\mathbf{x}) = \mathbf{f}_{\mathbf{CR3BP}}(\mathbf{x}) + \mathbf{f}_{\mathbf{GH}}(\mathbf{x}) = \mathbf{f}_{\mathbf{CR3BP}}(\mathbf{x}) + \begin{bmatrix} \mathbf{0_{3x1}} \\ \mathbf{a}_{\mathbf{G_2}}^{\mathbf{p}}(\mathbf{q}) \end{bmatrix} \tag{8}$$

$$\mathbf{a}_{\mathbf{G_2}}^{\mathbf{p}}(\mathbf{q}) = \mathbf{A}_{3B}^{BCBF}\left(\mathbf{A}_{TSE}^{BCBF}(\mathbf{q})\right)^T\nabla_{TSE}u_{G_2}(\mathbf{q}) \tag{9}$$

A related augmented Jacobi integral for the CR3BP-GH could be defined as in Eq. (2), simply expanding the complete gravity potential of Phobos with the GHs series.

Finally, it's important to recall that Phobos' orbit itself is highly non-Keplerian due to the strong Martian J_2 action, but this perturbation (still time-invariant due to Phobos' properties and the axial-symmetry of J_2) is not considered in our model, because in this paper we are interested in the relative dynamics near Phobos. Figure 3 (right) shows that the differential

Mars-J_2 perturbation is negligible inside the moon's SOI. In particular, the inclusion of the oblateness of the massive bodies in the CR3BP has been investigated in Douskos and Markellos (2006), Arredondo et al. (2012), Abouelmagd and Sharaf (2013): in addition to the direct gravitational effect, the inclusion of J_2 of the primary body affects also the apparent acceleration, by increasing the angular velocity of the frame of reference by a factor $\sqrt{1+\frac{3}{2}J_2(R_1/L)^2}$. The differential Mars-$J_2$ perturbation reported in Fig. 3 (right) includes also this action. Apparent effects of additional Mars' GHs are also negligible, as well as the ones of all Phobos' GHs inside the SOI. For our focus on the LPOs, the Mars–Phobos CR3BP-GH is therefore still defined with the time-scale of the unperturbed mean motion of the Keplerian, circular and equatorial orbit of Phobos around Mars.

2.4 The Mars–Phobos ER3BP-GH

Despite the fact that the orbital eccentricity $e = 0.0156$ of Phobos is not particularly high, it can be seen in Fig. 3 (right) that the differential perturbation has a significant effect on the LPOs, as an indirect effect of the collapse of the SOI's boundary towards the moon. The addition of the eccentricity in the CR3BP has already been investigated in the past (Szebehely 1967; Campagnola et al. 2008), and it has been extensively studied in an elliptic R3BP (ER3BP) in the same barycentric and rotating 3B frame of the circular case. The frame of the ER3BP rotates not uniformly, but with a time-varying ω and $\dot{\omega}$. Besides, the classical ER3BP uses a time-dependent length unit corresponding to the distance between the two massive bodies (called a pulsating frame), and a non-uniform time variable corresponding to the true anomaly ν.

In our case, since we are focused on studying close relative motion around Phobos, and also we need to include the GHs of the moon, the classical pulsating frame of the ER3BP is avoided, because it produces different time-dependent scalings for each GH at different degree, i.e. $(1+e\cos\nu)^{-n}$. To overcome this, the equations of motion of the Mars–Phobos ER3BP with the moon's GHs (named ER3BP-GH) are derived in Phobos' Hill's frame. This frame is still rotating with the Mars–Phobos elliptic motion $\omega = [0; 0; \dot{\nu}]$, but is centered at Phobos, and it uses the same fixed length unit L (semi-major axis) used for the previous models. Regarding the time variable, since the vectorfield is used not only for integration but also in continuation schemes in Sect. 3, the convenient choice is to consider a fixed time unit too, and use the mean anomaly. This is because the sensitivity of the flow with respect to ν_0 could be retrieved appending ν in the state vector $\mathbf{x} = [\mathbf{q}; \dot{\mathbf{q}}; \nu]$. Eq. (10) presents the equation of motion of the ER3BP-GH in the Phobos' Hill's frame.

$$\dot{\mathbf{x}} = \mathbf{f}_{\mathbf{ER3BPGH}}(\mathbf{x}) = \begin{bmatrix} \mathbf{0_3} & \mathbf{I_3} & \mathbf{0_{3x1}} \\ -\frac{(1+e\cos\nu)^4}{(1-e^2)^3}\mathbf{P} + 2\frac{(1+e\cos\nu)^3 e\sin\nu}{(1-e^2)^3}\mathbf{W} & -2\frac{(1+e\cos\nu)^2}{(1-e^2)^{3/2}}\mathbf{W} & \mathbf{0_{3x1}} \\ \mathbf{0_{1x3}} & \mathbf{0_{1x3}} & 0 \end{bmatrix} \mathbf{x} + \begin{bmatrix} \mathbf{0_{3x1}} \\ \nabla u_{G_1}(\mathbf{q},\nu) + \nabla u_{G_2}(\mathbf{q}) + (1-\mu)\frac{(1+e\cos\nu)^2}{(1-e^2)^2}\begin{bmatrix}1\\0\\0\end{bmatrix} \\ \frac{(1+e\cos\nu)^2}{(1-e^2)^{3/2}} \end{bmatrix} \tag{10}$$

It is worth noting that in this model the gravity potential of Phobos depends only on the relative position $\mathbf{q}$ in the Hill's frame, while all the other terms depend also on ν. In particular Mars' pulsating position along the x-axis is $x_1 = -(1-e^2)/(1+e\cos\nu)\ L$ units. It is easy to see that the model of Eq. (10) reduces to the circular cases of Eqs. (1), (8) for $e = 0$.

Summarizing the eccentricity produces a time-dependent perturbation to the dynamics of the circular case, and no integral of motion is available whatever reference frame is chosen to express the dynamics.

3 Computation of periodic and quasi-periodic LPOs and their dynamical substitutes

The invariant solutions of the dynamical systems of Eqs. (1), (8), (10) are trajectories that can be decomposed as the sum of n periodic functions, realizing an n-torus, such as equilibrium points (EPs, $n = 0$), periodic orbits (POs, $n = 1$), and quasi-periodic orbits (nD-QPOs, $n \geq 2$). The trajectory of a n-torus can be seen as dependent on n phases φ rather than time.

In this section we use the procedures of dynamical systems theory that define such invariant solutions to compute the LPOs of the Mars–Phobos-spacecraft system. First, we apply these techniques to the well-known case of the dynamics approximated by a CR3BP, to compute the classical LPOs in this system. These solutions are then used as starting guesses for the numerical continuation technique, that will be applied to find the dynamical substitutes of the LPOs in sequence, first in the CR3BP-GH, and then in the Mars–Phobos ER3BP-GH. The resulting orbits are collected in Sect. 4.

3.1 LPOs of the Mars–Phobos CR3BP

In this section we introduce the structure of the natural invariant motions near Phobos and how they are computed in the framework of the CR3BP of Eq. (1).

Equilibrium points The CR3BP is time-invariant therefore the stationary points of the effective potential of Eq. (2) are the five equilibrium points in the rotating frame (Koon et al. 2011): the three collinear Libration points (LPs), aligned with the two bodies (two close to the secondary, L_1 in inferior and L_2 in superior conjunction, as seen from the primary, and L_3 in opposition), and the two equilateral L_4 and L_5, equidistant from them and with elongation of 60° from both bodies.

The LPs are computed as roots of the vectorfield of Eq. (1) using Newton's method (Allgower and Georg 2003; Koon et al. 2011). The collinear couple L_{1-2} is very important in mission design, as their distance from the secondary formally defines its SOI. Figure 3 (left) shows the Hill's surfaces for the L_2 energy. Due to the small mass parameter, the energy difference between L_1 and L_2 is very small in non-dimensional units (10^{-8}), therefore the manifolds of the two LPs are almost symmetrical, and the location of L_{1-2} is close to the linearized approximation expressed by the Hill's SOI's radius (L_1 is at 16.582 km and L_2 is at 16.601 km from Phobos' barycenter). Regarding their stability properties, L_{1-2} are characterized by a vertical center manifold, and on the orbital plane by a center $\times$ saddle behavior, which is unstable. This means that the region of the phase-space around these LPs is characterized by two manifolds of periodic orbits, their IMs, and transit (inside the IMs) and non-transit (outside them) orbits between the realms of attraction of the two bodies (Koon et al. 2011).

Periodic orbits Since the CR3BP is time-invariant, the two center manifolds of periodic orbits around each LP are organized in two 1-parameter families at increasing size and energy from them, called planar and vertical Lyapunov orbits (Koon et al. 2011). As their energy increases, they encounter bifurcations: the first one of the planar orbits gives birth to

the two symmetrical branches (with respect to the x–y plane) of Northern and Southern Halo orbits (Koon et al. 2011; Gómez and Mondelo 2001); the second one of the planar orbits gives birth to the two symmetrical branches (with respect to the x-axis) of axial orbits that represent a two-lane bridge to the first bifurcation of the vertical orbits (Gómez and Mondelo 2001); further bifurcations provide multiplication of the orbits' period (Gómez and Mondelo 2001).

Analytical and semi-analytical methodologies, such as the Lindstedt–Poincaré techniques (Koon et al. 2011; Masdemont 2004; Hou and Liu 2011), allow high-order approximations of the nonlinear dynamics to compute periodic and quasi-periodic solutions of a dynamical system. They can provide very accurate initial conditions to propagate in the full nonlinear dynamics, but if the POs are highly unstable even very high-orders do not have a very extended region of convergence (Koon et al. 2011; Masdemont 2004; Gómez and Mondelo 2001). In these cases, numerical methodologies must be applied to provide reliable solutions for practical applications, where low-order analytical solutions are used as starting guesses (Gómez and Mondelo 2001). Such techniques search for an initial condition of a PO applying its definition as an equilibrium fixed point of a stroboscopic map (for time-variant systems) or a Poincaré map (for time-invariant systems) (Koon et al. 2011) in a classical Newton's method. Thus, the numerical methodology requires the integration of the equations of motion and the associated variational equations at each step of Newton's method. This procedure is commonly known as a differential corrector (Stoer and Bulirsch 1983), or shooting method, and referred to as single shooting for the case when only one trajectory is propagated at each iteration, and multiple shooting when N independent trajectories are propagated at each iteration of the differential corrector.

The families of Lyapunov orbits of the Mars–Phobos CR3BP are computed in this paper using the Lindstedt–Poincaré method. The method approximates the nonlinear terms of the gravity potential as a series expansion of Legendre polynomials, and computes the coefficients of the series expansion of only the periodic normal modes of these approximated dynamics (Koon et al. 2011; Masdemont 2004). The two families of Halo orbits are computed through the numerical differential corrector (Koon et al. 2011; Gómez and Mondelo 2001; Howell 1984). The Poincaré map is taken at the surface of section $g(\mathbf{x}) = y$, and due to the symmetries of the CR3BP, the objective function is to erase the final velocities $\dot{x}$ and $\dot{z}$ correcting the initial state x and $\dot{y}$. The initial guess for the differential corrector is given by Richardson's solution (Richardson 1980), which is a Lindstedt–Poincaré expansion at order 3. These four families of POs around each LP have been computed up to the intersection with Phobos, and they are all unstable as described by Floquet theory (Koon et al. 2011; Howell 1984). Further bifurcation branches, in particular the one of the axial orbits, are not considered due to the collapse of the SOI of this system, as they are placed after the intersection with Phobos. Figure 4 shows some example of POs that we computed using these methods in the Mars–Phobos CR3BP.

Quasi-periodic orbits The double center manifold of the CR3BP is then characterized by families of 2-tori, which are quasi-periodic orbits with two phases, at increasing size around each PO with central part. Due to the pattern of the projections on the coordinate planes, they are referred as Lissajous orbits (Koon et al. 2011). Each PO constitutes the backbone of a family of iso-energetic QPOs: on the map where the initial condition of the PO represents an invariant point, each iso-energetic 2D-QPO represents an invariant closed curve.

In this paper, the manifold of the 2-parameter family of Lissajous orbits around the Lyapunov orbits is computed directly with the Lindstedt–Poincaré expansion of 2-tori (Koon

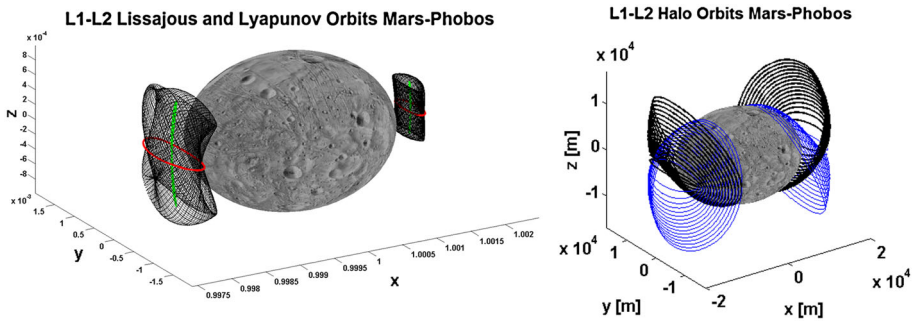

Fig. 4 LPOs in the Mars–Phobos CR3BP. On the *left* example of two planar (*red*) and vertical (*green*) Lyapunov orbits around each LP and one Lissajous (*black*) orbit of high width around them. On the *right* families of Northern (*black*) and Southern (*blue*) Halo orbits. Mean ellipsoid for Phobos surface. From this point, axes in all the figures are normalized in L units unless otherwise indicated

et al. 2011; Masdemont 2004). These orbits are all unstable as described by Floquet theory (Koon et al. 2011). Figure 4 shows examples of QPOs computed in the Mars–Phobos CR3BP.

Invariant manifolds Finally, the presence of the saddle manifold implies that the LPOs are separatrices of motion between transit and non-transit orbits to enter or escape from the SOI of the second massive body. The boundary of these tubes is given by the IMs of the LPOs that provide the energy efficient trajectories to minimize the fuel consumption of spacecraft for interplanetary transfer phases (Koon et al. 2011; Conley 1969). The local direction of the IMs is represented by the eigenvectors of the set of hyperbolic eigenvalues of the linearized dynamics of the LPO. There are two kinds of IMs: the linear span of the stable eigenvectors along the orbit and the one of the unstable set, and each of them has two branches, defined by the sign of the eigenvector. For each saddle manifold, to derive the complete tube of each of the four branches, one should integrate the initial conditions provided by the IM along the orbit and derive the set of trajectories. This procedure is known as the globalization of the manifold and it has been widely applied in the CR3BP (Koon et al. 2011; Gómez et al. 1991).

In this paper, due to the proximity of the LPOs to Phobos, all the inside branch of their IMs intersects Phobos, therefore no homoclinic nor heteroclinic connections of the two LPs manifolds exist. In Sect. 5.4 we compute the inside branch of the IMs of the LPOs in the ER3BP-GH and derive the performances of these natural trajectories to arrive (along the unstable IMs) and depart (along the stable IMs) from the moon's 3D surface.

3.2 Dynamical substitutes of the LPOs

This paper focuses on the computation of the natural orbits in close proximity of Phobos. Due to the collapsing effect of its SOI, these are the families of periodic and quasi-periodic LPOs computed in Sect. 3.1. However, in Sect. 2.2 we found that the CR3BP does not provide a suitable approximation of the relative dynamics, which in this region should take into account two important orbital perturbations. This led us in Sects. 2.3 and 2.4 to define two additional dynamical models, the CR3BP-GH that encloses the modeling of the gravity field of the moon with GHs, and the ER3BP-GH that considers Phobos moving in an elliptical orbit around Mars. The procedure that we present in this section is to use the LPOs of the CR3BP as starting solutions of a numerical continuation along the three different dynamics,

computing in sequence their dynamical substitutes in the new models. A dynamical substitute, as the name suggests, is the equivalent of the classical solution of the original dynamics in a perturbed dynamical system, and was introduced in Gómez et al. (2002). The dynamical substitute is an orbit that not only is a solution of the new dynamics, but also maintains in its phase-space the natural and forcing frequencies of the perturbation.

The numerical continuation is a well-known numerical technique used to compute the curve of solutions of a parametric nonlinear equation (Keller 1977; Allgower and Georg 2003). This method starts from a known solution of the equation, which is at a value of the parameter that makes it simpler to solve analytically or numerically. The numerical continuation consists in incrementing the parameter slowly, solving Newton's methods by iteratively using, as an initial guess, the solution found at the previous step, until the solution for the desired value of the parameter is obtained. In this paper the numerical continuation is applied to find EPs, POs, and QPOs solutions of differential equations, therefore the continuation parameter weights the level of perturbation between different dynamics, and at each step the related differential correction scheme to compute the invariant solution is performed. Since the nonlinear effects of the perturbation could be significant, to overcome possible turning points in the continuation curve the numerical continuation is implemented with the pseudo-arclength algorithm (Keller 1977; Allgower and Georg 2003). Also, to enhance the convergence of the differential corrector and speed up the continuation, we use a predictor for the initial guesses of the differential corrector along the continuation curve, and an adaptive step strategy based on the control of the number of Newton's method iterations (Allgower and Georg 2003; Masdemont and Mondelo 2004).

3.2.1 Dynamical substitutes of the LPOs in the Mars–Phobos CR3BP-GH

In this section we present the approach used to compute the dynamical substitutes of the LPOs from the model of Eq. (1) to the system described by Eq. (8). We differentiate the procedure undertaken by the phase-space dimension of the invariant solutions, which are EPs, POs, and 2D-QPOs. As the perturbation of Phobos' GHs is time-invariant in the 3B frame, the dynamical substitutes of the invariant solutions maintain the dimension of their original phase-space in the CR3BP.

Equilibrium points The EPs of the CR3BP-GH are calculated similarly to the CR3BP, with the potential function of Eq. (2) now considering the complete gravity field of Phobos through Eq. (5), without need of numerical continuation. Also, it must be reported that the truncated GHs model mathematically provides additional EPs to the system, but they are not useful as will be discussed in Sect. 4.1.

Periodic orbits To derive the substitutes of the periodic LPOs in the Mars–Phobos C3BP-GH, the numerical continuation is used starting from the initial conditions of the families of POs computed in the basic CR3BP. The differential corrector scheme's step looks for invariant points of a Poincaré map. The continuation parameter is, intuitively, a scaling factor σ_{GH}, from 0 to 1, to weight the GHs acceleration in the intermediate vectorfield $\mathbf{h}$.

$$\dot{\mathbf{x}} = \mathbf{h}\left(\mathbf{x}, \sigma_{GH}\right) = \mathbf{f}_{\mathbf{CR3BP}}\left(\mathbf{x}\right) + \sigma_{GH}\mathbf{f}_{\mathbf{GH}}\left(\mathbf{x}\right) \rightarrow \phi_{\mathbf{h}}\left(t, t_0, \mathbf{x}_0, \sigma_{GH}\right) \tag{11}$$

The problem is conservative and an appropriate Jacobi integral of the augmented vectorfield is available as was addressed in Sect. 2.3. Therefore, POs are continued in a differential way with respect to the state of the current LP, using a variant Poincaré map $g(\mathbf{x}, \sigma_{GH}) = y - y_{LP}(\sigma_{GH})$, and with a fixed-energy constraint with respect to the energy of the LP. As the

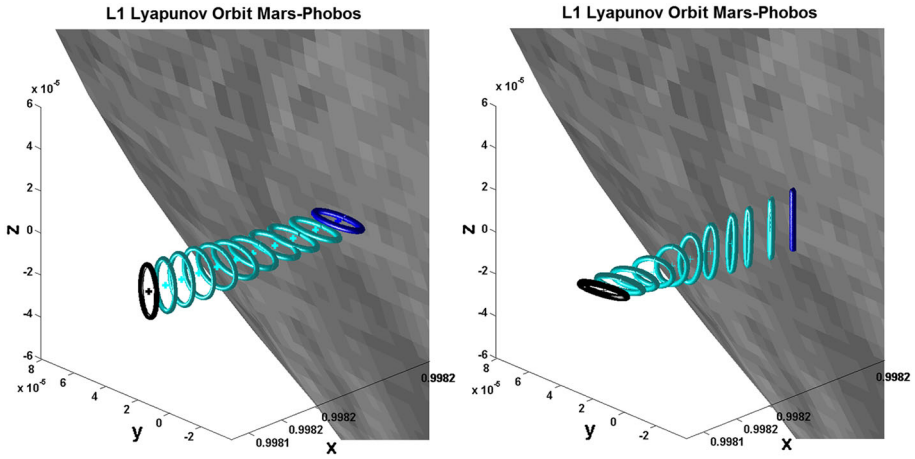

Fig. 5 POs in the Mars–Phobos CR3BP-GH. Numerical continuation with respect to the GHs of a small-energy planar and vertical Lyapunov orbit around L_1 of the CR3BP (*blue*) to their dynamical substitute in the CR3BP-GH (*black*) belonging to the families A and B respectively, together with the current LP

two dynamics have different Jacobi integrals, the dynamical substitute is naturally identified as the orbit with the same energy gap $\Delta c(\mathbf{x}) = c(\mathbf{x}) - c(\mathbf{x}_{LP})$ from the energy level of the LP in the related dynamics. Therefore, the numerical continuation of the POs embeds also the computation of the current LP: this choice of a differential numerical continuation has been proved to be 33 % faster than continuing the absolute state, since it requires less differential corrector iterations for a given step size.

The numerical continuation is performed for a sampling of POs for each of the four families of the CR3BP, for both LPs. Figure 5 shows what "physically" happens: as σ_{GH} is increased from 0 to 1, the small planar and vertical Lyapunov orbits follow the corresponding LP and are highly distorted, mostly in the second half of the continuation. In particular, the vertical Lyapunov orbit deploys itself in a 2:1 elliptical orbit too, and counterintuitively, substitutes of planar orbits are mostly vertical and substitutes of vertical ones are mostly planar at $\sigma_{GH} = 1$. These results demonstrate the effect of the strong 3D-coupled dynamics. In this sense, the Hessian of Eq. (7) applied in Eq. (9) maintains the decoupling of the x-y and z dynamics of Eq. (8), when linearized around L_{1-2}, only for even zonal harmonics or sectorial harmonics. It is worth noting that with this continuation scheme, turning points of the continuation curve are present: planar Lyapunov and Northern and Southern Halo orbits of the CR3BP are linked together under the framework of the augmented state space $[\mathbf{x}; \sigma_{GH}]$ of the vectorfield $\mathbf{h}$.

After obtaining this sampling of dynamical substitutes, the new families of POs in the CR3BP-GH can be visually identified, and will be discussed in Sect. 4. To refine the families of POs identified with this approach, we then take one of the POs just computed for each of them and perform a numerical continuation with respect to the differential Jacobi integral Δc used as a fixed constraint previously, in the final CR3BP-GH for $\sigma_{GH} = 1$.

Quasi-periodic orbits To compute the families of 2-tori around each PO of the families with central part of the CR3BP-GH, we used the numerical approach of dynamical systems theory that derives the invariant curve of these QPOs on an iso-energetic Poincaré map. This invariant object provides a closed curve of initial condition for the surface of motion, and it is described by the truncated Fourier series $C^F(\mathbf{c}, \theta)$ function of the curvilinear coordinate θ,

and the Fourier coefficients $\mathbf{c}$ ($2N_C + 1$ for each coordinate variable). Different differential corrector schemes based on Fourier analysis have been used, see Gómez and Mondelo (2001), Kolemen et al. (2012), Olikara and Scheeres (2012). In this paper the approach of Kolemen et al. (2012) is adopted, where the curvilinear coordinate that parameterizes the invariant curve is the polar anomaly between two state components. Since the invariant curve is continuous, it is discretized in N_S sample points. The differential corrector consists of a multiple shooting scheme that forces the images of the sample points through the Poincaré map to lie on the same Fourier series C^F, by fine tuning the Fourier coefficients in a least mean square (LMS) fitting algorithm. The gap between the curvilinear coordinates of image and initial condition along the invariant curve constitutes its rotation number profile; for the nonlinear CR3BP-GH, this is not flat and unknown a priori. As the CR3BP-GH is time-invariant, the family of iso-energetic invariant curves around a PO backbone is obtained embedding the LMS algorithm in a numerical continuation with respect to a sizing parameter of the curve. Once one invariant curve is identified, it's possible to simulate the QPO by numerically integrating through iterative mappings, interpolating the intermediate initial condition along the invariant curve; this is necessary also to derive its rotation number profile. These surfaces of motion represent the dynamical substitutes of the Lissajous orbits of the CR3BP around Lyapunov and Halo orbits.

To perform the stability analysis for QPOs and the computation of the related IMs, we modified the method of Kolemen et al. (2012) in order to provide a 1–1 mapping that determines the invariant curve in a way that resembles the invariance condition of POs. This lies in the fact that we approximate the invariant curve with a truncated Fourier series expansion. The idea is that the set of mappings of the initial conditions along the starting curve $C^F(\mathbf{c}_0, \theta)$ constitutes a second curve that could also be defined by a related set of final Fourier coefficients $\mathbf{c}_f$. This is a map from a set of Fourier coefficients to another (at the same truncated order), and if the curve is invariant under the usual map, the initial Fourier coefficients $\mathbf{c}_0$ are a fixed point of the new map. In this case, moving from sampled points (the set of final conditions) to coefficients, the discrete Fourier transform is used to define the new map, which is solved using LMS because the images' sampling is not uniform. The complexity has been transferred to the map itself, because the same LMS algorithm is now embedded inside it and no longer required to solve the linear system of the Newton's method iterations, which is now characterized by a square Jacobian matrix. Indeed the map of the new method requires the computation of the full inverse of a large-scale left pseudo-inverse matrix with dimension $(2N_C + 1)$, requiring far more computational time than the previous one. However it provides, as a byproduct, a monodromy matrix for the stability analysis of the QPO. The related eigenvalues for an invariant curve are organized in circles on the complex plane (Jorba 2001; Adomaitis 2007), and the Floquet linear stability is therefore given by their magnitude. Their eigenvectors are defined in the space of the Fourier coefficients, therefore they provide a curve of initial conditions for the globalization of the IMs.

3.2.2 Dynamical substitutes of the LPOs in the Mars–Phobos ER3BP-GH

In this section we present the approach used to compute the dynamical substitutes of the LPOs from the model of Eq. (8) to the one of Eq. (10). The ER3BP-GH is a time-variant dynamical system, sum of its conservative vectorfield (the CR3BP-GH in the Hill's frame) plus a forcing term (the elliptic perturbation). The general solution of such ODEs is constituted by its homogeneous term (sum of the normal modes of the conservative part) plus a particular solution (dependent from the kind of forcing term). The elliptic perturbation on the CR3BP-GH, as we see in Eq. (10), is function of ν, and it is a periodic signal at the orbital frequency

of the primaries: the particular solution is a signal at the same frequency. This means that the solutions of the elliptic dynamics in the phase-space have one phase constrained to follow the dynamics of $\nu(t)$, which is appended in the vectorfield and so explicitly retrievable from the integration of the equations of motion. The vectorfield of the ER3BP-GH is a natural homotopy $\mathbf{h}$ with respect to the eccentricity

$$\dot{\mathbf{x}} = \mathbf{f}_{\mathbf{ER3BPGH}}(\mathbf{x}) = \mathbf{h}(\mathbf{x}, e) \rightarrow \phi_{\mathbf{h}}(t, t_0, \mathbf{x}_0, e) \tag{12}$$

and the numerical continuation with respect to the eccentricity of the invariant solutions computed in the CR3BP-GH increments by one their phase-space and produces dynamical substitutes in the ER3BP-GH that oscillate around the original ones with period 2π.

Periodic orbits Since the dynamics of the ER3BP-GH are time-variant, and the eigenvalues of the LPs of the CR3BP-GH are different from the orbital frequency of Phobos, no physical EPs exist in this non-pulsating system. The LPs now become POs, as they oscillate along the LPs of the circular case.

Apart from the dynamical substitutes of the ancestor EPs, isolated POs in the ER3BP-GH develop when the original PO in the circular case is resonant with ν. In this case, the characteristic curves of the period of the POs for the families of the CR3BP-GH show us in Sect. 4.2 that one family around each LP has one PO with period π, which is the usual overresonance 2:1 (resonances with high denominators are not considered). The dynamical substitutes of these two synchronous POs in the ER3BP-GH are still POs, with period 2π: this gives rise to two iso-periodic families of POs in the elliptic problem, since the circular problem is a singular case for the definition of ν_0. The computation of these POs could be undertaken with the differential corrector used previously in Sect. 3.2.1 for POs, but using a stroboscopic map with propagation time of 2π, and embedded in a numerical continuation where the parameter is the eccentricity. This approach was first undertaken in Broucke (1969), to compute dynamical substitutes of POs from CR3BP to ER3BP. This continuation produces different dynamical substitutes starting from different ν_0 on the same stroboscopic map. Single shooting was used in Broucke (1969) to compute only symmetrical dynamical substitutes, starting the continuation only at pericenter or apocenter conditions. For our asymmetric ER3BP-GH, the curve of initial conditions on the stroboscopic map is required. In particular, due to the overresonance, one half of this curve could be avoided, since the initial conditions correspond to the flows starting from the other half after a time of π.

2D quasi-periodic orbits Tori with two phases are the dynamical substitutes of the POs of the CR3BP-GH in the general non-resonant case. They are derived with the differential corrector that computes their invariant curve, used previously in Sect. 3.2.1 to compute families of 2-tori around a PO in the CR3BP-GH, but with some important differences. First, the invariant curves are now defined on a stroboscopic map, with the period fixed to the one of the original PO. Second, the invariant curve parameter is fixed to be ν on the stroboscopic map, so the related return value after one revolution is directly retrievable by integration of the equations of motion. Third, the only constraint to add regards the longitudinal phase indeterminacy of the torus (Gómez and Mondelo 2001). The initial condition of the PO computed in the CR3BP-GH is translated to Phobos' Hill's frame of its circular orbit around Mars, and then the differential corrector is embedded in a numerical continuation with respect to the eccentricity to find the invariant curve in the ER3BP-GH. An example is shown in Fig. 6 (left). This procedure has already been used in Olikara and Scheeres (2012) to find dynamical substitutes of periodic LPOs from CR3BP to ER3BP. Once a QPO is obtained, the refinement for the related family can be achieved by changing the continuation parameter to be the

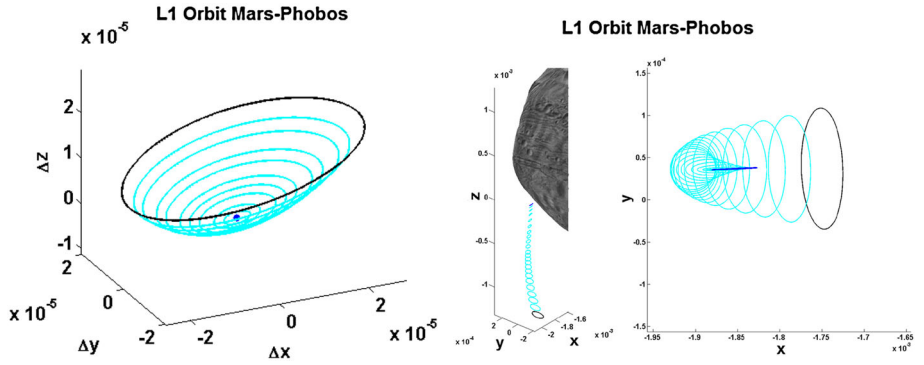

Fig. 6 *Left* QPOs in the Mars–Phobos ER3BP-GH. Numerical continuation of the invariant curve on the stroboscopic map with respect to the eccentricity, from a medium-energy PO of the A family around L_1 of the CR3BP-GH (*blue point*) to the dynamical substitute in the ER3BP-GH (*black*). *Right* QPOs in the Mars–Phobos ER3BP-GH. Numerical continuation of the invariant curve on the stroboscopic map with respect to the stroboscopic period, from a low-size QPO (*blue*) to the QPO intersecting Phobos' surface (*black*) of the A family around L_1 in the ER3BP-GH

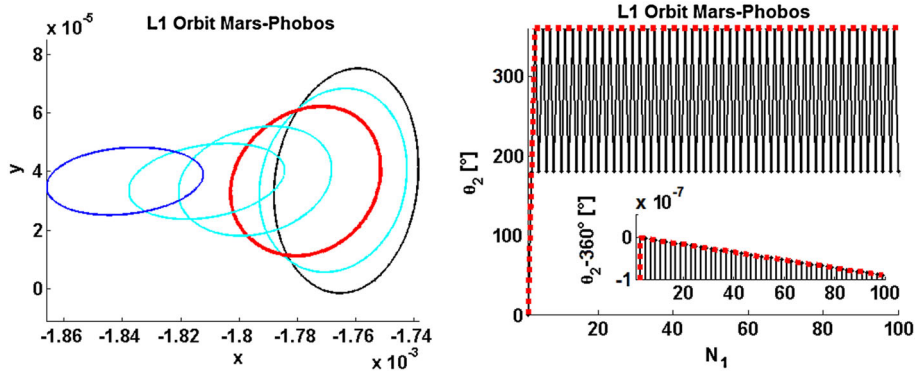

Fig. 7 QPOs in the Mars–Phobos ER3BP-GH. On the *left* invariant curves on the stroboscopic map of the D family around L_1, from a low-size QPO (*blue*) to the QPO intersecting Phobos' surface (*black*). The invariant curve *highlighted in red* corresponds to a QPO with the resonant stroboscopic period π. On the *right* the related profile of the curve's parametrization variable (corresponding to Phobos' true anomaly) along iterated mappings shows that the profile at the second-return frequency (*red*) is flat: as the magnification highlights, the total change of the Phobos' true anomaly is just 10^{-7} ° in 100 stroboscopic periods, therefore this QPO constitutes a closed family of POs in the ER3BP-GH, since every point along the curve is invariant

stroboscopic time, in the final ER3BP-GH with the eccentricity of Phobos. An example of this second scheme is shown in Fig. 6 (right).

This algorithm for QPOs naturally embeds the resonant cases N:M: when the period of the ancestor PO is in an integer ratio M:N with the orbital period, the invariant curve of its dynamical substitute on a multiple-return stroboscopic map (propagation time of N times the orbital period) has a flat rotation number profile, whose value is zero. Therefore this method for QPOs is used to continue the two synchronous POs in 2:1 resonance of the CR3BP-GH, and it is clearly superior to the dedicated one of Broucke (1969) for POs, because it provides not only one initial condition in the ER3BP-GH, but directly a curve of invariant points that describes the iso-periodic family of POs, as shown in Fig. 7.

3D quasi-periodic orbits Tori with three phases are the dynamical substitutes of the QPOs of the CR3BP-GH, and each of them is identified by an invariant 2-torus. The differential corrector method for computing QPOs is naturally extended to a phase-space with higher dimensions using a multi-dimensional Fourier series to describe the invariant object. However, for an ER3BP this is high computationally demanding. In this paper, to conclude the analysis of the manifold of LPOs in the ER3BP-GH, we used the differential corrector scheme, embedded in a numerical continuation with respect to the eccentricity, of the classical multiple shooting (Masdemont and Mondelo 2004; Stoer and Bulirsch 1983) that satisfies the continuity between the subintervals where the QPO trajectory is sampled for a finite propagation time. The resulting linear system of the differential corrector is in this case underdetermined, and the solution at each step is taken as the one with the minimum norm correction. This does not guarantee to find a bounded orbit for high perturbations, since the solution is not a dynamical substitute. However as Fig. 8 shows, the orbits obtained oscillate around the ancestor 2D-QPOs with an amplitude similar to that of the LPs even for a high time span set in the differential corrector. Therefore we conclude that such trajectories describe appropriate 3-tori in the defined time span, which in terms of number of longitudinal revolutions is longer than that of typical applications of LPOs in mission segments. The IMs are obtained from the hyperbolic eigenspace of the state-transition matrix within each subinterval.

4 LPOs around Phobos and analysis of the results

In this section the LPOs obtained with the methodologies described in Sect. 3 are presented and analyzed. The related performances for potential station-keeping applications are collected in Sect. 5.

4.1 Dynamical substitutes of the equilibrium points and Hill's surfaces

The collinear EPs L_{1-2} of the classical CR3BP represent the first two intersections of the Hill's surfaces at increasing energy: L_1 between the realms of admissible motion around Mars and Phobos, and L_2 between the exterior realm around both bodies and the realm around Phobos. This holds for the Mars–Phobos CR3BP-GH. However, the additional terms of the GHs in the augmented potential definition of Eq. (2) have an energizing effect on the Phobos realm, so the two intersections occur farther away from Phobos. Another effect of the GHs is to create additional lobes on the Hill's surface. They are evident at the "birth" of the realm (which is at low energy), and as the energy increases the Hill's surfaces grow in dimension and their lobes collapse with each other. This continues until there are no more lobes nor residual internal holes and the realm becomes "adult", which is at an energy such that the Hill's surfaces tend to the ones of the classical CR3BP. The points where the surfaces attach to each other are additional EPs of the model. An example is shown in Fig. 9 for the case of only adding J_2 to the CR3BP, where two additional and symmetrical EPs are born in the x-z plane, close to the z-axis of Phobos' Hill's frame and slightly pointing towards Mars. The result for a generic CR3BP with the addition of J_2 for either one or both primaries was first indicated in Douskos and Markellos (2006). These points are usually inside the central body's figure. This is also the case in our system with GHs up to fourth degree. The four additional equilibria are not valid because interior, with the outermost located 2 km below Phobos' surface. The "adult" realm, once the last additional EPs is born, will then intersect the Hill's surfaces of the Martian and exterior realms to provide the new LPs of the CR3BP-GH. Table 2 provides the location of the dynamical substitutes of these LPs, and Fig. 10

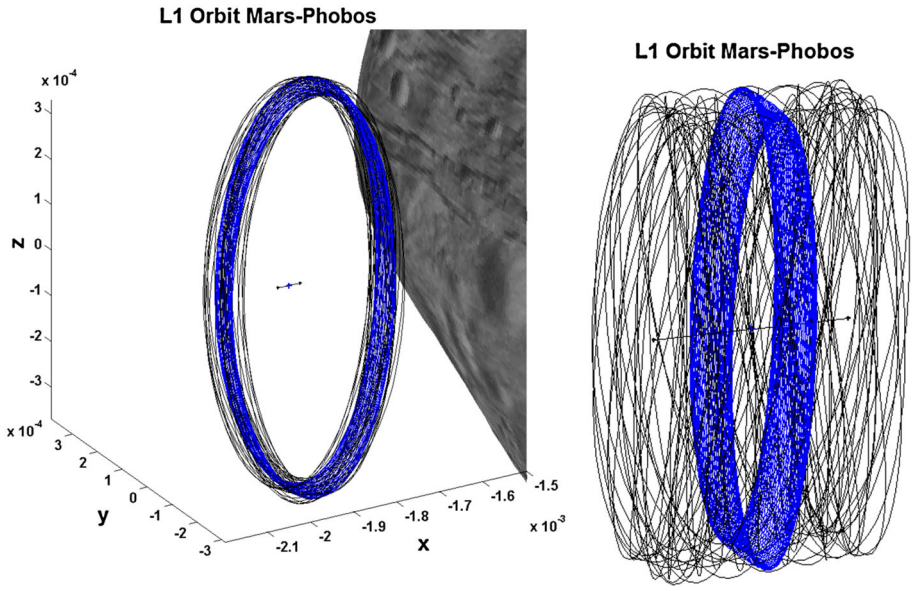

Fig. 8 3-Tori in the Mars–Phobos ER3BP-GH. Example of a small-width and medium-size 3D-QPO of the A family (*on the left*) and of a large-width and low-size 3D-QPO of the A family (*on the right*), both around L_1 of the ER3BP-GH. The 3D-QPOs in *black*, obtained by multiple shooting of the 2D-QPOs of the CR3BP-GH in *blue*, oscillate around these backbones with an amplitude equal to the motion of the LP in the ER3BP-GH, also plotted in the *graph*. Integration up to the first transversal revolution of the backbone 2D-QPO in the CR3BP-GH

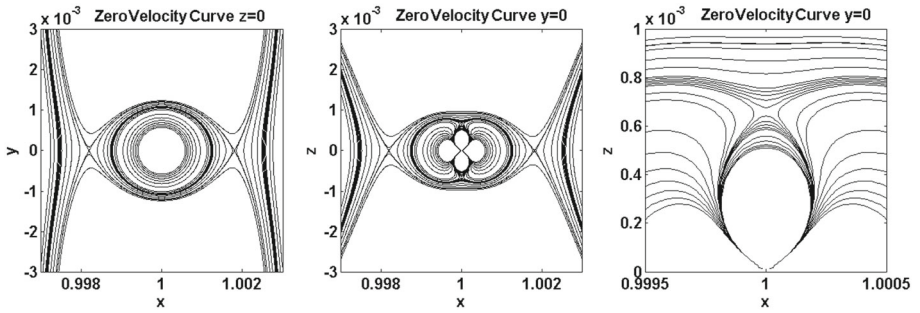

Fig. 9 Hill's surfaces in CR3BP-J_2 at different energies. x–y and x–z projections, with magnification around Northern additional EP

shows the pattern of the Hill's surface at the energy of L_2. Due to the low mass parameter, as it was in the CR3BP, the energy difference between L_1 and L_2 is small in non-dimensional units (10^{-7}), therefore the related Hill's surfaces at the energy of L_1 and L_2, apart from the small region around each EP, are practically unchanged: they identify the boundary of the Hill's SOI. The asymmetric displacement of L_1 and L_2 from their original values in the basic CR3BP model is significant, and accounts for 20 % of their altitude over Phobos. This shows how inaccurate the CR3BP is for practical applications.

Note in Fig. 10 that the Hill's surfaces at the energy of the LPs around Phobos are very close to its surface. This was already evident in a classical CR3BP, just considering a mean ellipsoid

Table 2 CR3BP-GH collinear equilibria

EP	Δx (m)	Δy (m)	Δz (m)
L_1	−743	346	−195
L_2	643	345	−101

Displacement of the LPs of the CR3BP-GH from their original value in the CR3BP

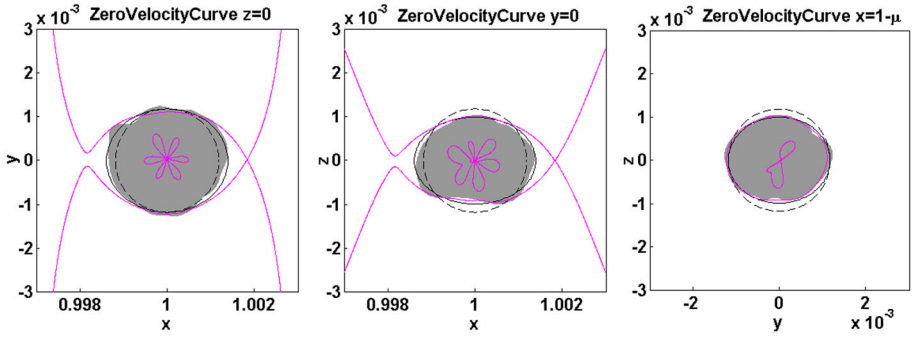

Fig. 10 Hill's surface in CR3BP-GH for L_2 energy. Projections on coordinates planes. Phobos real shape, mean sphere (*dashed line*) and ellipsoid (*plain line*)

as reference from the Phobos' shape as shown in Fig. 3 (left). However, the inclusion of the GHs improves the correspondence between the two boundaries in particular in the vertical dimension, where no other way of escape at low energy is available because the gateway of the IMs of the LPs is close to the orbital plane. The fact that the body's shape fills entirely its SOI is considered one of the proofs of the theory of accretion proposed by Craddock (2011) [see also Rosenblatt and Charnoz (2012)] to explain the origin of Phobos, in contrast to the asteroid capture (Rosenblatt 2011; Lee 2012; Koschny 2012). The theory of accretion speculates that a previous small body impacted Mars; the ejecta from the red planet created a ring of dust around Mars, that eventually built up to create Phobos. The results obtained with our enhanced CR3BP-GH suggest that the transportation of mass at low energy could be responsible for the current shape of Phobos, in particular for the vertical dimension. An additional consideration on the range of dimensions of these transferred materials will be presented in Sect. 5.5.

The properties of L_{1-2} are an important summarizing figure to conduct a convergence analysis on the CR3BP-GH as a function of the number of GHs. This is done incrementally increasing the terms of the series expansion included in the dynamics. Using the benchmark model of Martinec et al. (1989) as a reference, we see in Fig. 11 that convergence under 2 % is achieved at degree and order 4 for the static location of the LPs. Considering the dynamical properties, an even better convergence is achieved for the eigenvalues and the saddle's eigenvectors, which represent the direction of the IMs. For the eigenvectors of the two centers the outcome depends on the components. Identifying each center manifold as the state-space's section around the LP where each family of POs develops, the same figure of convergence is achieved for the in-section components, while the out-of-section components are still oscillating at high amplitude, in particular over 10 % for L_2. Therefore the outcomes are mostly accurate for the IMs and the longitudinal behavior of an invariant motion, while a more refined model is needed for the quasi-periodic motion around them.

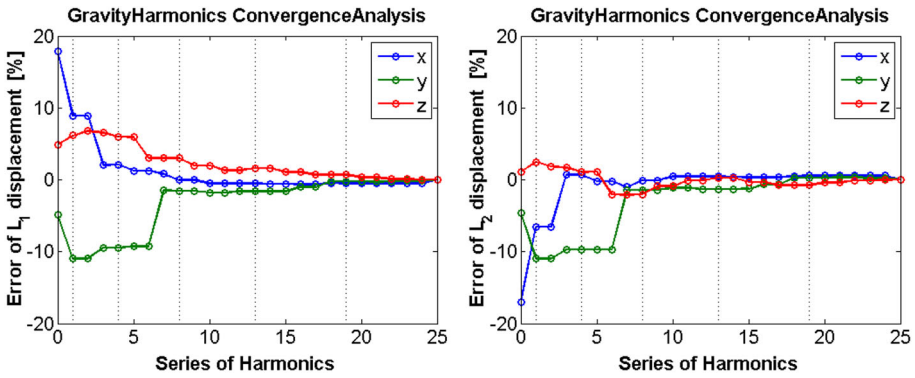

Fig. 11 Convergence analysis of the CR3BP-GH. L_1 and L_2 displacement from the original value in the CR3BP. *Error* respect to the solution with all the harmonics is normalized by the altitude over Phobos' surface. *Dotted lines* refer to increasing zonal harmonics degree starting from J_2

Finally, the dynamical substitutes of the LPs in the ER3BP-GH are POs, similar to 1D oscillations around each LP of the CR3BP-GH, with an amplitude of 260m, which is significant at the length scale of Phobos for practical applications, and a direction tilted from the x-axis by effect of the GHs: they can be seen in Fig. 8. It is well-known that in the ER3BP the EPs and the related Hill's surfaces move with the pulsating reference frame, therefore the concept of a pulsating SOI for Phobos can be extended also to the ER3BP-GH. This could be simulated considering the two extreme phases of Phobos at perimars and apomars, changing the length unit to rescale the non-dimensional CR3BP-GH. The difference from the classical ER3BP is that the outcomes of the non-dimensional circular problem are not maintained at different phases of Phobos, and should therefore be recomputed because the pulsating length unit provides a different scaling of the GHs (as pointed out in Sect. 2.4). However at the L_2 energy, the Hill's surfaces obtained at the extreme phases are similar to the ones of the CR3BP-GH, therefore the eccentricity effect does not seem to be a relevant factor for the accretion theory's validation.

4.2 Dynamical substitutes of the periodic orbits

The periodic LPOs of the Mars–Phobos CR3BP are the 1-parameter families of planar and vertical Lyapunov orbits and Northern and Southern Halo orbits. They have been computed with classical semi-analytical and numerical techniques, and an example is shown in Fig. 4.

The dynamical substitutes of these POs in the CR3BP-GH are obtained with the continuation schemes discussed in Sect. 3.2.1, and they are showcased in Fig. 12. They are constituted by two 1-parameter families A and B originating from each LP, and by a detached 1-parameter family CD, made by two branches C and D connected by a common orbit at the lowest energy. The low-energy orbits of the families A and B are highly distorted from their ancestor Lyapunov orbits in the CR3BP as we see in Figs. 5 and 13, because the highly inhomogeneous gravity field of Phobos produces a 3D coupled linearized state-matrix at the LP. Besides, the force field at the LP is no longer symmetric and highly tilted from the one of the classical CR3BP, and the structure of the saddle × center × center manifolds is no longer aligned with the coordinates axes and planes. The orientation of the centers' manifolds is given by the couples of "relative inclination / ascending node's right ascension" of each family's small-energy PO. Around L_1, family A has 46°/278°, family B has 82°/98°, and around L_2, family A has

26°/43°, family B has 71°/223°. Interestingly, the two POs around each LP have opposite nodes (see also Fig. 13). The effect of the complex gravity field of Phobos is mostly local and is therefore averaged for larger orbits, that resemble the shape of the LPOs of the classical CR3BP. The shape of larger orbits of the family A is similar to the Southern Halo, B to the planar Lyapunov, C to the Northern Halo, and D to the vertical Lyapunov. However, the tilt is still maintained, and this represents the most significant effect of the addition of the GHs of the second massive body. This information can be evaluated from the eigenspace at the LP. Regarding the properties of these new POs, the period is close to the natural one of the LP as shown in Fig. 14, and the Floquet stability analysis presented in Fig. 15 shows that all the orbits are unstable. The families A and C, like the Halo orbits, have their maximum stability index s_λ (Howell 1984) (a measure proportional to the instability) that rapidly decreases with increasing size of the orbit; the maximum s_λ for the family B is less sensitive to the size; the branch D is instead characterized by a saddle × saddle × center manifold, therefore no QPOs exist around these POs.

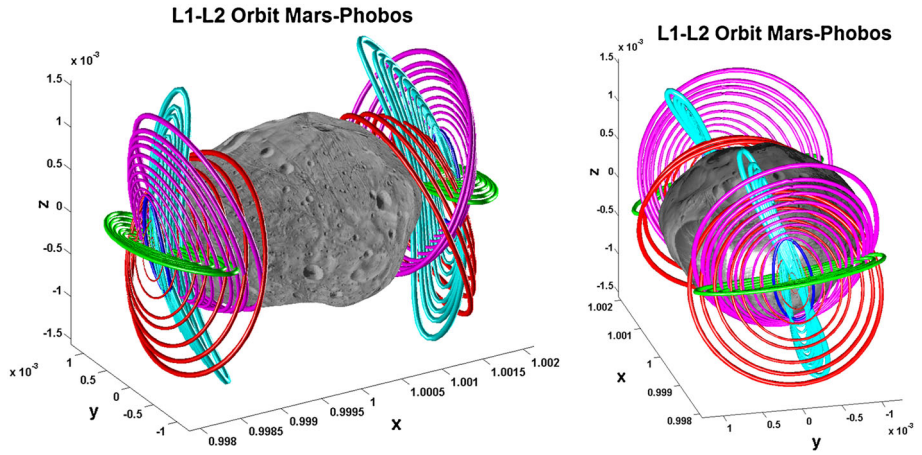

Fig. 12 Periodic LPOs in the Mars–Phobos CR3BP-GH. Graphical visualization of the new A (*red*), B (*green*), C (*magenta*), and D (*cyan*) families of POs around each LP in the CR3BP-GH. Shape harmonics series expansion for Phobos' surface

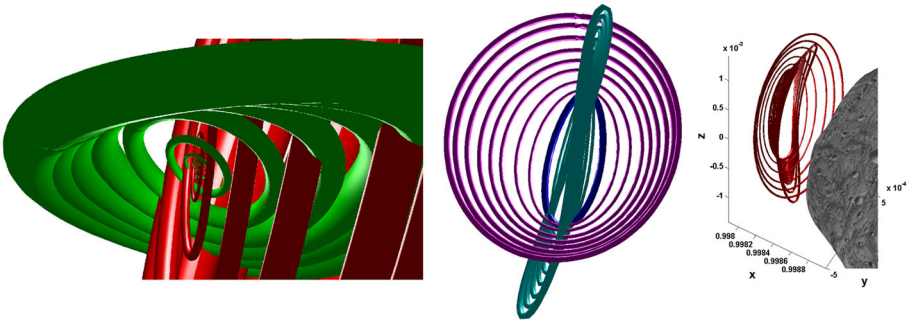

Fig. 13 Periodic LPOs in the Mars–Phobos CR3BP-GH. On the *left* behavior of the A and B families around L_1 at low energy. On the *right* behavior of the C and D families around L_1 showing their actual connection through the ancestor orbit (*in blue*) as two branches of a single CD family

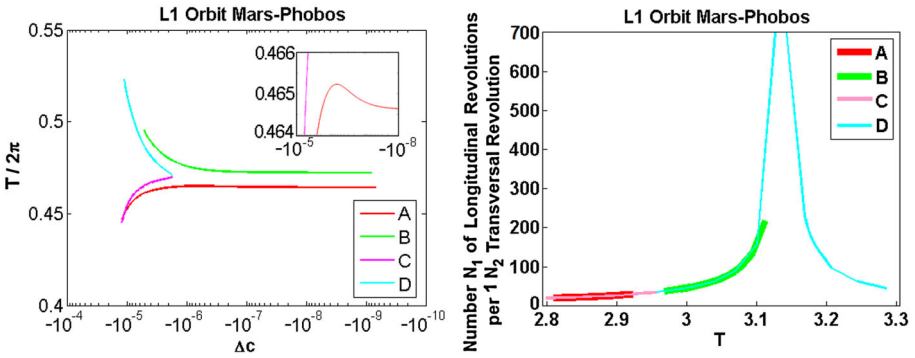

Fig. 14 LPOs characteristic curves. On the *left* characteristic curves of the period of the families of POs around L_1 in the CR3BP-GH, parameterized by the non-dimensional differential Jacobi integral with respect to the LP. Magnification shows that the family A's characteristic curve is not monotonic. On the *right* characteristic curves of the period of the first transversal revolution around the invariant curve on the second-return stroboscopic map of the families of 2-tori around L_1 in the ER3BP-GH, parameterized by the non-dimensional stroboscopic period. The asymptote for the D family at the synchronous period $T = \pi$ corresponds to the 2:1 resonant QPO that is actually a family of POs

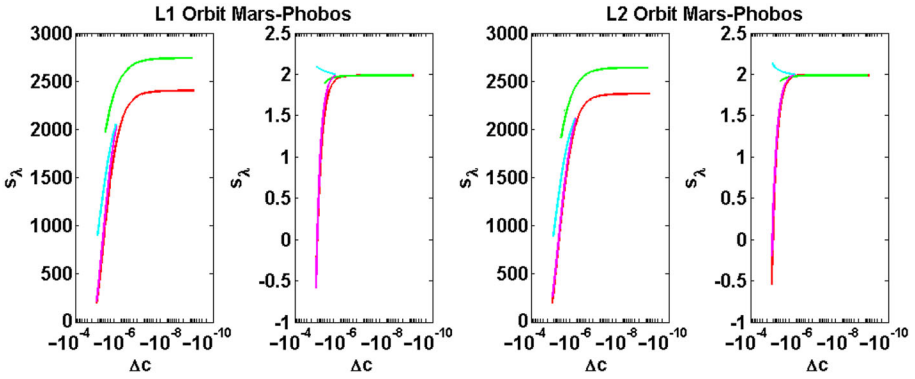

Fig. 15 LPOs stability properties. Characteristic curves of the stability indexes of the two non-unit couples of eigenvalues of the monodromy matrix of the families of POs in the CR3BP-GH, parameterized by the non-dimensional differential Jacobi integral with respect to the LP. Families' colors are coherent with Fig. 12

As explained in Sect. 3.2.1, the families of periodic LPOs in the CR3BP-GH have been obtained with two continuation schemes. The first uses as continuation parameter the GHs' magnitude σ_{GH} to derive the dynamical substitute of a PO from the original CR3BP, and the second uses as continuation parameter the energy Δc to compute the family of POs in the CR3BP-GH. With this second continuation scheme, we found that the families C and D are actually two branches of the same global family CD, since they are connected through an ancestor orbit at the lowest energy as we see in Fig. 13. In particular the reverse numerical continuation of this ancestor orbit with the first scheme, from $\sigma_{GH} = 1$ to the original CR3BP for $\sigma_{GH} = 0$, produces as continuation curve a closed loop, which does not provide a dynamical substitute in the original CR3BP at the same energy Δc. We underline that a similar procedure to compute the POs in the CR3BP-GH could be undertaken by-passing the first scheme by computing analytically the LPOs in the linearized dynamics of Eq. (8), which represent the dynamical substitutes of the small Lyapunov orbits showed in Fig. 5. After, the

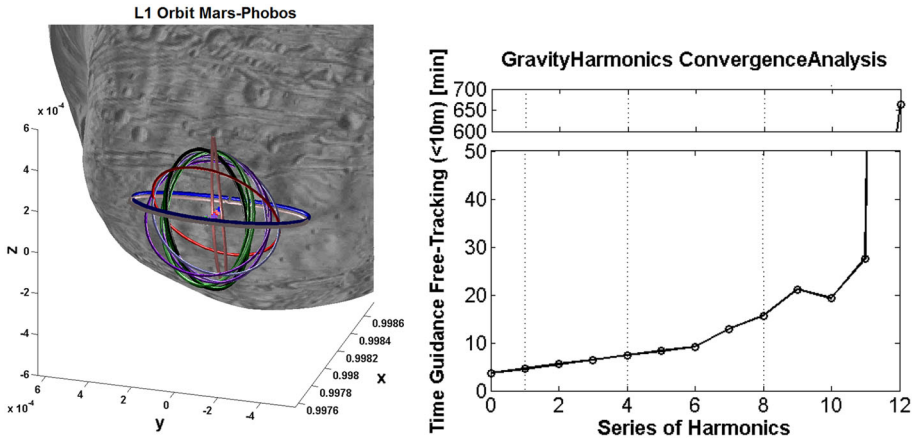

Fig. 16 Convergence analysis of the LPOs in the Mars–Phobos CR3BP-GH. The figure on the *left* shows the different dynamical substitutes of a medium-energy planar Lyapunov orbit around L_1 of the CR3BP (*blue*), obtained incrementally increasing the degree and order of the harmonics included in the partial CR3BP-GH (*red* for degree 2, *purple* for degree 3, *green* for degree 4, with *color darkened* by increasing order, and final orbit at fourth degree and order in *black*). Crosses represent the current EP. On the right, related time such that the flow of these solutions in the full CR3BP-GH remains within a position error of 10m from their reference signal. *Dotted lines* refer to increasing zonal harmonics degree starting from J_2

second scheme is performed from these solutions. This allows to compute the families A and B, but not CD, which would require a bifurcation analysis. However, the profile of the stability indexes of the three families in Fig. 15 does not suggest that the family CD bifurcates from neither A nor B, even with a bridge of POs at high-energy intersecting Phobos' figure. The strategy of two continuation schemes in cascade allowed us instead to compute easily the family CD, where the first scheme finds a PO "seed" to feed the second.

Finally, we investigated the convergence of the numerical continuation procedure, as a function of the degree and order of the Mars–Phobos CR3BP-GH, as was done in Sect. 4.1 for the EPs. One sample medium-energy orbit of the A family has been chosen to evaluate the cost of the different truncated models in Fig. 16. Compared to the case of the EPs, the outcome is that a worse convergence of 5 % is achieved for both static and dynamical properties, in particular regarding the center manifold longitudinal to the PO. To have an idea of the price to pay, we simulated the dynamical substitutes found at each different degree and order in the complete CR3BP-GH up to degree and order 4. Considering the data at degree and order 3, station-keeping at a frequency of more than ten times per LPO's period is required to track the reference signal within 10m.

The dynamical substitutes of the POs in the ER3BP-GH are still organized in the same 1-parameter families A, B, and CD, but now they are constituted by invariant 2-tori with one phase set to be the true anomaly of Phobos around Mars, and are showcased in Fig. 17. The width of their invariant curves, obtained with the continuation schemes discussed in Sect. 3.2.2, is comparable to the LP oscillation's amplitude. Simulating these QPOs by multiple-return stroboscopic maps, the rotation number profile of the transversal phase around the invariant curve is obtained. This allows us to determine how many longitudinal revolutions are needed to achieve a full lap of the invariant curve, and is presented in Fig. 14. This number increases when the period of the ancestor PO tends to be in an integer ratio with the orbital period. In particular, in Fig. 14 we see that large 2D-QPOs of the families B and D in the

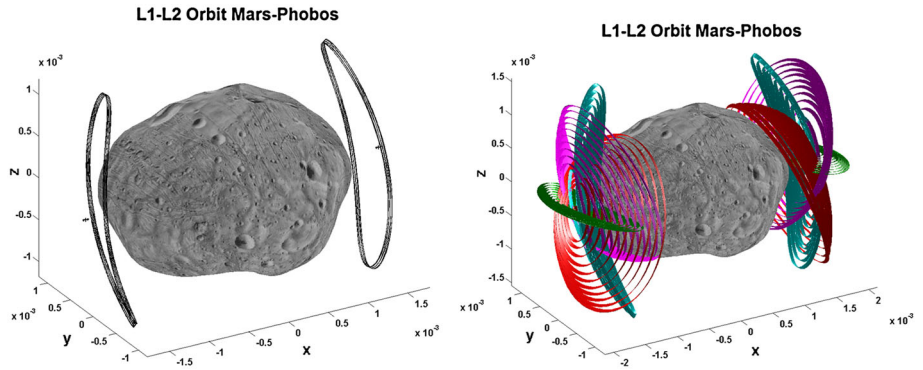

Fig. 17 LPOs in the Mars–Phobos ER3BP-GH. On the *left* the two iso-periodic families of POs around the oscillating LPs. On the *right* the families of 2-tori: A (*red*), B (*green*), C (*magenta*), D (*cyan*)

ER3BP-GH are close to the resonance 2:1, therefore after two revolutions the spacecraft will fly back near the initial condition. For the family B around each LP, the POs with period π slightly intersect Phobos, therefore are not considered in this paper. For the synchronous case of the family D, the invariant curve is resonant as presented in Figs. 7 and 17 shows the large, vertically-elongated, inclined POs, similar to eight-shaped orbits, that exist in the ER3BP-GH around both sides of Phobos.

4.2.1 Sensitivity analysis and tracking performance of the LPOs in the ER3BP-GH

The POs of the family D in the ER3BP-GH are chosen to conduct a first-order sensitivity analysis to assess the effect of the uncertainties of the modeling parameters, navigation sensors, and the physical perturbations in tracking the reference signal of the orbit computed. The initial condition of this reference trajectory is propagated in the perturbed dynamics, and the error of the resulting flow from the reference signal is computed. Two metrics are used to assess the tracking performance: the position error from the guidance law after a prescribed propagation time, and the time that the flow freely tracks the reference signal within a prescribed position error. Thus, two thresholds are introduced. The prescribed propagation time is set to be one tenth of the Mars–Phobos (and the PO itself) orbital period, as this is close to the reference value of 44min required for a transponder's signal's round-trip at the farthest Earth–Mars distance. The prescribed position error is set to be 10m, as this is close to the value of 10^{-6} L units commonly used for the Sun–Earth and Earth–Moon systems (Koon et al. 2011). Figure 18 presents the analysis for several parameters, normalized in abscissa by the sensitivity number S. For semi-major axis a, mass parameter μ, eccentricity e, GHs' coefficients, and initial condition $\mathbf{x}_0$ of relative position and velocity, S weights these uncertainties with respect to the related reference value of the ER3BP-GH. For the other actions, 1rad is used for the initial true anomaly ν_0, the mean motion (equal to 1/time unit) for the angular velocity ω of the BCBF frame, 1/(time unit)^2 for its angular acceleration $\dot{\omega}$, 1.90° as the maximum tilt θ between BCBF and Hill's frames, the Phobos gravity at the SOI's boundary for the magnitude of a harmonic perturbing acceleration a^P at the orbital frequency. Furthermore, the GHs model of Martinec et al. (1989) is used as a benchmark representing a more realistic dynamical model of the spacecraft around Phobos, to relate the sensitivity of the other perturbations. This test indicates that station-keeping is required at least every 17min for the POs around L_1. In this sense, not including the GHs would have

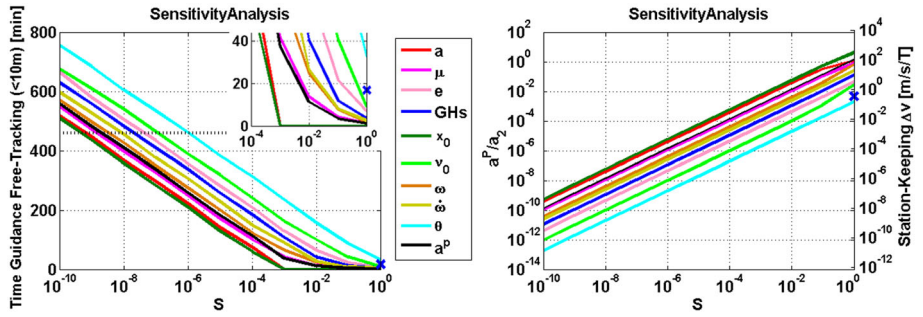

Fig. 18 Sensitivity and performance analysis of the LPOs in the Mars–Phobos ER3BP-GH. The first figure shows the propagation time where the spacecraft remains within the error of 10m from the reference signal of one PO of the D family around L_1 in the ER3BP-GH, when propagated in perturbed dynamics where the modeling parameters, navigation inaccuracies, and physical forces in the legend are weighted by the sensitivity factor S. The *blue cross* represents the benchmark dynamics. The *horizontal dotted line* is the PO period. The second figure shows the related equivalent perturbing acceleration (normalized by the Phobos gravity at L_1) that produces the same final response as a constant input in a forced undamped unstable 1D oscillator. The second ordinate axis represents the associated Δv consumption over one period

required maintenance actions at least every 4min, while not including the eccentricity would have required station-keeping at least every 7min. The savings on the duty cycle are 76 and 58 % respectively, which highlight the importance of including these forces in the dynamical model to design orbits around Phobos.

The second conclusion arises from the comparison of the sensitivity of the perturbations. In Sect. 2.3 we estimated that in our ER3BP-GH, the residual perturbations of both the benchmark dynamics and the frame's libration motion account for a few percent of the cumulated GHs perturbation at the SOI, which itself is of the order of 10^{-1} of the Keplerian gravity [see Fig. 3 (right)]. This first estimation is now confirmed for the LPOs computed in the ER3BP-GH, as the results of the benchmark and the maximum tilt in the first graph of Fig. 18 fall within the ones of an additional relative perturbing acceleration a^P between 10^{-3} and 10^{-2}, and an inaccuracy of μ of the same range. Inaccuracies of the semi-major axis and the relative non-dimensional state are similar, and very sensitive (inaccuracies over 6×10^{-4} produce initial errors larger than the 10 m threshold), while inaccuracies of the true anomaly and rotational rates of the frame are allowed to be higher. Summarizing, the first graph of Fig. 18 provides the maximum inaccuracies: if the parameters are acquired within these inaccuracies, station-keeping at the frequency of the time threshold chosen will maintain the spacecraft within the deadband defined by the position threshold required. Relative inaccuracies larger than 3×10^{-4} for a, 9×10^{-4} for μ, 3×10^{-2} for e, 9×10^{-3} for GHs' coefficients, 2×10^{-4} for $\mathbf{x}_0$, 9×10^{-2} for ν_0, 3×10^{-3} for ω, 5×10^{-3} for $\dot{\omega}$, 6×10^{-1} for θ, 8×10^{-4} for a^P, require the control load every 44min to be increased, or the guidance performance of 10m to be relaxed. In particular, we see that the value for ω is larger than the perturbation on the mean motion of the Hill's frame introduced by Mars J_2, which is 2×10^{-4}, confirming that this term could be disregarded from our model as explained in Sect. 2.3.

It is now possible to plot these actions deriving an associated figure of perturbing acceleration, in order to universally compare the sensitivity effects with the preliminary orbital perturbations analysis in Fig. 3 (right). This is done with an equivalent model that considers only the unstable normal mode, which is responsible for the drift of the perturbed trajectory from the reference signal. In the 1D linear ODE $\ddot{x} - \omega_0^2 x = a^P$, the state x represents the

magnitude of the position error from the reference signal, and the natural pulsation ω_0 is taken as the maximum unstable Floquet exponent of the PO (2.26 of the mean motion). The system is forced by the constant acceleration a^P, and the analytical solution is available. Thus, the equivalent constant acceleration that produces the same final response of the numerical simulation is computed for every perturbing action, and is presented in the second graph of Fig. 18, in terms of the same ratio a^P/a_2 used in Fig. 3 (right). The two cases (response at prescribed propagation time and at prescribed position error) have produced a similar output, so the graph refers to the first one. For a linear approximation comparison, related Δv consumptions over one period are indicated in parallel. The LPO computed in our model would require 0.5 m/s per period in the more accurate GHs and maximum-misaligned model, that constitute the main residual perturbations assuming the remaining model parameters and navigation variables are acquired within the following relative and absolute inaccuracies: 5×10^{-4} for a (5 km), 4×10^{-3} for μ(10^3 m^3/s^2 for Phobos' GM and 9×10^{10} m^3/s^2 for Mars' GM), 10^{-1} for e (2×10^{-3}), 4×10^{-2} for GHs' coefficients, 4×10^{-4} for $\mathbf{x}_0$ (6m for relative position and 2×10^{-3} m/s for relative velocity), 3×10^{-1} for ν_0 (20°), 10^{-2} for ω (2×10^{-6} rad/s), 2×10^{-2} for $\dot{\omega}$ (10^{-9} rad/s^2), 3×10^{-3} for a^P (8×10^{-6} m/s^2). This represents a considerable saving from the 11 and 3.2 m/s per period if, respectively, the GHs and eccentricity are not included in the dynamical model.

4.3 Dynamical substitutes of the quasi-periodic orbits

The quasi-periodic LPOs of the Mars–Phobos CR3BP are the 2-parameters families of Lissajous orbits around every Lyapunov and Halo orbit that do not intersect Phobos. Examples of QPOs computed with the Lindstedt–Poincaré algorithm are shown in Fig. 4.

The 2D-QPOs in the CR3BP-GH have been derived with the numerical technique that computes their invariant curve around the backbone PO as discussed in Sect. 3.2.1. This differential corrector scheme allows to directly compute all the family of iso-energetic QPOs in the final dynamics, so no continuation between different models is required. Similarly to the CR3BP for the two Lyapunov families, the 2-tori of the families A and B are connected to each other because they are part of the same 4D center manifold originating from the EP, as shown in Fig. 19. Simulation of the QPOs by iterative mappings allows to display the surfaces of toroidal motion presented in Figs. 19 and 20, as well as retrieve the rotation number property. Cases of resonances with high denominator are present.

Finally, a sampling of these QPOs has been continued to consider the additional forced phase introduced by the elliptic dynamics, as discussed in Sect. 3.2.2. As shown in Figs. 8 and 20, the motion in the ER3BP-GH oscillates around the solution found in the circular case with an amplitude similar to the one of the LPs.

The families of QPOs in the CR3BP-GH and ER3BP-GH are all unstable, and all the inside branch of their IMs intersects Phobos' surface, which is modeled by the high-order shape harmonics model. The exploitation of the IMs in the ER3BP-GH is undertaken in Sect. 5.4.

5 Applications of the LPOs and their invariant manifolds

In this section we present the performance of the LPOs computed in Sect. 4, as well as their IMs, with respect to a number of potential applications that can be required in the design of a space mission to Phobos.

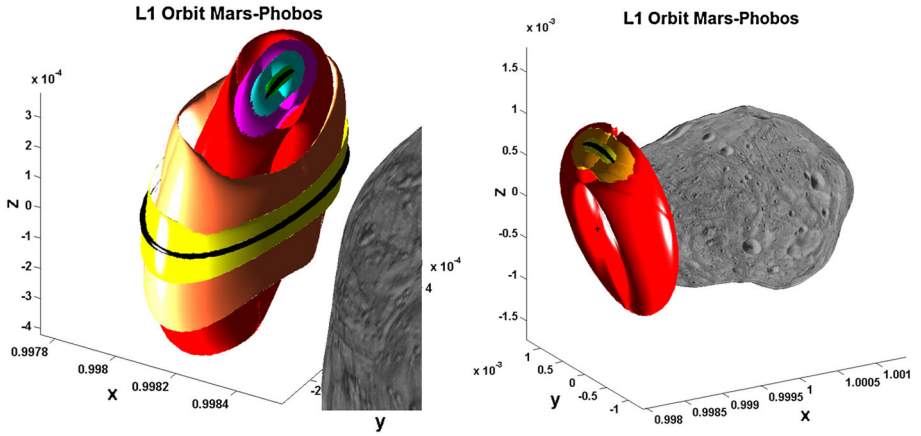

Fig. 19 Quasi-periodic LPOs in the Mars–Phobos CR3BP-GH. On the *left* graphical visualization of the family of QPOs that connects the two medium iso-energetic POs of the A and B families around L_1 of the CR3BP-GH. Related two backbones POs displayed in *black*. On the *right* family of QPOs around a medium-energy PO of the C family around L_1 of the CR3BP-GH

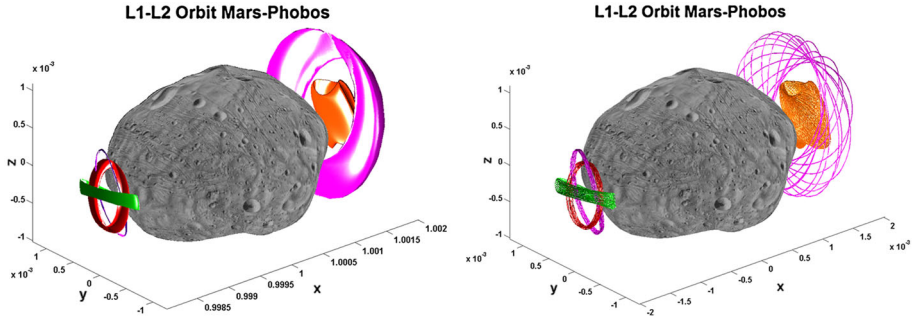

Fig. 20 LPOs in the Mars–Phobos CR3BP-GH and ER3BP-GH. Graphical visualization of 2-tori in the CR3BP-GH (*on the left*) and related 3-tori's orbits in the ER3BP-GH (*on the right*), of different size and width around the LPs. Summarizing examples: three medium-size QPOs of family AB (*red* and *green* with small-width, *orange* with high-width) and two high-width QPOs of family C (of small and large-size)

5.1 Lighting conditions

The kinematics of the Sun are included in the rotating frame of the R3BP to evaluate the instantaneous field of view of the Sun for a point around Phobos. As the tilt between the equatorial planes of Mars and Phobos is approximated to zero, the orbital plane of the R3BP is inclined with respect to the Solar ecliptic plane by Mars' rotational tilt $\theta_M = 25.2°$. The Sun position vector in the rotating frame rotates clockwise with an angular velocity equal to the difference between Phobos and Mars revolution rates (dominated by the first), with a fixed declination in the range $[-\theta_M, \theta_M]$ according to the seasonal phase of Mars. Seasons of Phobos correspond with Mars' ones, so are referred without any distinction. Due to Mars' high eccentricity, seasons are unequal, with the Northern Hemisphere of Mars and Phobos experiencing a summer longer than that occurring in the South.

The analysis of the lighting conditions in this system is undertaken using eclipse modeling, which is to derive the zones of light and shadow produced by Mars and Phobos when

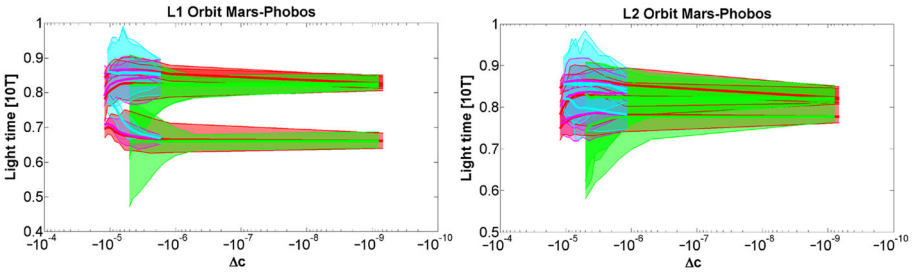

Fig. 21 LPOs lighting conditions. Light function of the families of POs of the CR3BP-GH (parameterized by the non-dimensional differential Jacobi integral with respect to the LP), averaged over 10 PO periods, at the days of equinoxes (*lower cluster*) and solstices (*upper cluster*). *Filled area* spans values for different starting phases of the Sun (*thick line* is for mean values), where families' colors are coherent with Fig. 12

illuminated by the Sun. This is described by a scalar light function field L, ranging from 0 to 1 to express the ratio of incident light with respect to the complete light case. For both Sun–Mars and Sun–Phobos couples the analysis could be undertaken with a cylindric model for the positions inside and close to the SOI's boundary of the moon. The shadowing wake of Phobos is limited by the size of the body, while Mars' wake covers all Phobos' neighborhood during an equinoctial season for 12 % of the orbital period, but its effect becomes null at the solstices. Also, as the revolution period of the Sun is almost double that of the LPOs, the average condition for points around L_1 and L_2 is to remain mostly in light, with the L_1-side experiencing more shadow time with the exception of the two solstice's seasons.

The analysis is undertaken for the POs of the CR3BP-GH, since they provide the backbone of both the QPOs in the same dynamical model and the QPOs in the ER3BP-GH, and the outcomes are presented in Fig. 21. Due to the additional phase of the Sun, we define the light function of the LPO averaging over 10 revolutions of the trajectory, and results will depend on the initial condition of the Sun around Phobos.

As presented in Fig. 21, medium-small LPOs within the families are similar to close-range hovering points on the two L_{1-2}-sides of the moon and the dependence of the Sun phase is mild (less than 5 %). Such LPOs of the families A and B are more exposed to light during the solstices than the equinoxes. At the equinoxes, all large orbits of the families A, B, and C experience more lighting time on the L_1-side, while the ones of A and C on the L_2-side experience more shadowing time than their medium-size orbits. Instead both families D experience more lighting time. At the solstices, more shadowing/lighting is obtained by the family A/C in summer, and by C/A in winter, while the families B and D are not altered by the type of solstice. The light time of large LPOs, if used for short operations, can be tuned accordingly to the Sun phase along Phobos, with the families B and D allowing to increase/decrease the mean light function up to 15 %.

5.2 Surface coverage

One of the most important requirements for an observation mission is the region of the surface that the instruments can point while the spacecraft moves along the chosen orbit. Figure 22 collects the regions of full geometrical coverage for the larger LPOs of every family of POs in the CR3BP-GH around both LPs. Thus, these outcomes consider no technical constraints and data of the instruments, such as the minimum elevation angle on the ground and the maximum angles of view that define the field of view of the instrument around its beam's boresight. The results are obtained using the high-order Phobos' shape harmonics.

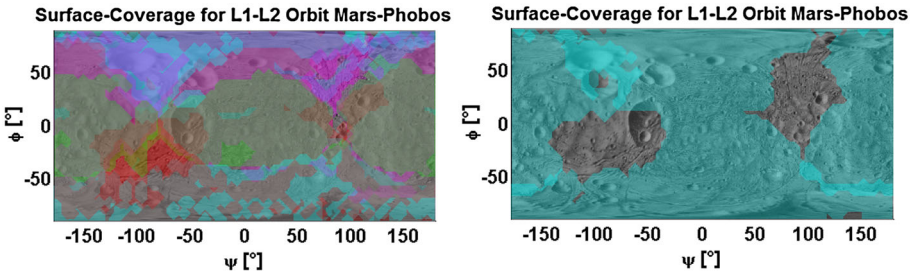

Fig. 22 LPOs surface coverage. On the *left colored areas* fill the regions of full geometrical coverage on Phobos' surface of the largest orbits of the families of POs around L_1 and L_2 of the CR3BP-GH. Families' colors are coherent with Fig. 12. On the *right* surface coverage of the synchronous POs of the family D around L_1 and L_2 of the ER3BP-GH

The family B provides the least surface coverage of all the families, allowing to point only at the regions on the cis (L_1) and trans (L_2) side of the moon, and covering respectively 28 and 31 % of the whole surface during a full orbit. The large POs of the family D, which are vertically-elongated and inclined, allow to cover both Poles and also a fair region on the leading and trailing-side of the moon, resulting in a 45/43 % coverage ratio. Finally, the families A (47/44 %) and C (39/39 %) cover the South and North polar sides respectively, and most importantly the leading and trailing-sides. Figure 22 shows that the union of the areas provided by all the families covers the whole surface. In particular, a combination of a large D orbit and an A or C orbit on the other side, as well as one A and one C on each side, could fill most of the map. Finally, Fig. 22 shows the surface coverage of the D families of POs of the ER3BP-GH. This case is very interesting because the orbits are synchronous, and the combined surface coverage is 73 % missing only two sectors on the leading and trailing-sides. A constellation, using a minimum of one spacecraft on each side, would enable a stationary communications bridge between most of the opposite sides of the moon (cis/trans, North/South, part of lead/trail) where different human crews or rovers could be displaced, as well as repeated access times to equatorial and middle latitude sites on Mars.

5.3 Radiation shielding

In this section we consider the possibility that a manned spacecraft during a Mars orbital mission segment could exploit Phobos as a natural and passive shield against the isotropic cosmic rays, whose hazardous radiation is currently considered the showstopper in designing a safe manned mission in deep space (Genta et al. 2014). The idea is that the fluence of the incoming isotropic particles (Galactic Cosmic Rays and part of Solar Energetic Particle Events) on a spacecraft is lowered proportionally to the filling fraction in the sky of the apparent size of the body's bulk, as seen by the spacecraft's location. In this paper we refer to this action as sky occultation. The computation is similar to the full geometrical coverage undertaken in Sect. 5.2, just considering the solid angle covered by Phobos (representing its apparent shape) instead of the footprint's area on its surface. Thus, the occultation function field O is the filling ratio of this area with respect to the background sky of 4π sr.

As in Sect. 5.1, the analysis in Phobos neighborhood considers also the effect of Mars, whose bulk provides a constant occultation of 3.4 % in the rotating frame of the R3BP. This effect is weighted by the Mars–Phobos light function, where Mars is the radiating body and Phobos is the central body. Unlike the Sun–Mars and Sun–Phobos couples, this light function

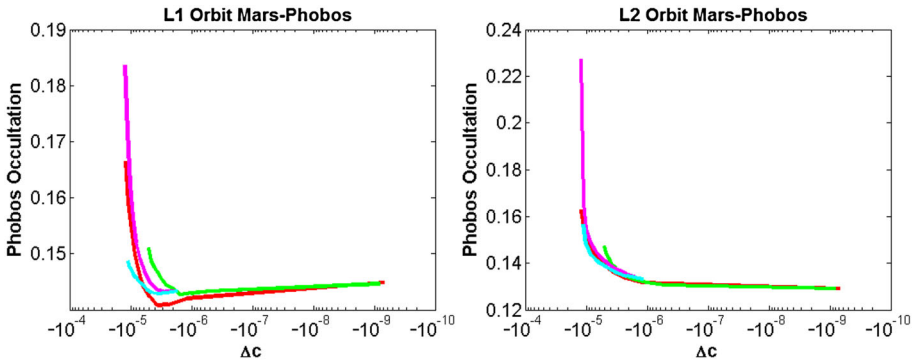

Fig. 23 LPOs occulting conditions. Sky occultation function by the Phobos' bulk of the families of POs around L_1 and L_2 of the CR3BP-GH (parameterized by the non-dimensional differential Jacobi integral with respect to the LP), averaged over 1 PO period. Families' colors are coherent with Fig. 12. Additional occultation by Mars' bulk will be 3.4 % on the L_1-side

must be computed with the accurate dual-cone model, since due to the proximity of Mars, the shadow cone's vertex of Phobos is located only at 2.77 Phobos mean radii in the anti-Mars direction. Therefore, the combined occultation is a few percent greater for LPOs on the L_1-side of the moon, than on the L_2-side. The major effect is indeed given by Phobos' bulk, and due to their proximity to Phobos, the sky occultation produced by the natural LPOs is relevant. Figure 23 shows that larger LPOs around both L_{1-2} can provide passive radiation shielding from over 20 % of the incoming isotropic cosmic rays. This result is obtained using the high-order shape harmonics model for Phobos' bulk.

5.4 Natural landing and take-off

Since the LPOs are close to Phobos, no homoclinic nor heteroclinic connections are available to naturally move around it, because all the inside branch of their IMs intersect Phobos. This is a unique feature of the Mars–Phobos CR3BP, because the natural trajectories, at low energy, to transfer between the SOIs of the two primaries in the Sun–Earth and Earth–Moon systems fly far from the bodies. In Baoyin and McInnes (2006), a selection of the smallest planar Lyapunov orbits whose IMs naturally intersect the smallest primary of the Sun–Earth and Earth–Moon systems, and provide whole-coverage along the body's orbital equator, has been undertaken. These orbits are very large and so require high energy relative to the one of L_{1-2}, and the analysis undertaken is 2D. The same approach could be extended considering impulsive propulsion to modify the IMs at the starting point at the LP (Baoyin and McInnes 2006) or along a smaller orbit, as well as including low-thrust continuous propulsion to modify directly the LPO. Instead in our unique case, a spacecraft could land or take-off from Phobos using the gateway of small-energy LPOs and with no need of thrust. In this section we find the landing and take-off sites on the 3D surface of Phobos and derive the performances at the touch-down and launch that are naturally provided by these trajectories.

The inside branch of the unstable and stable IM of the families of POs and QPOs of the ER3BP-GH has been computed with the techniques tailored for each invariant object introduced in Sect. 3, and propagated in the related dynamics up to the intersection with Phobos' surface modeled with the high-order shape harmonics model. Examples of these tubes are shown in Fig. 24, while the region of possible landing and take-off topographical

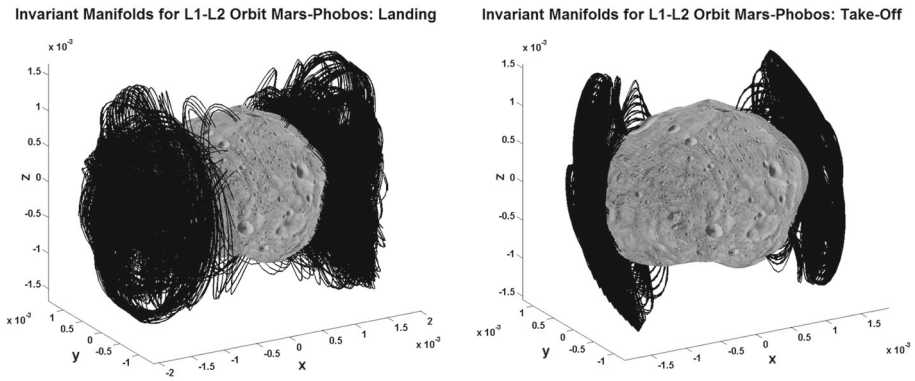

Fig. 24 IMs of the LPOs in the Mars–Phobos ER3BP-GH. On the *left* inside branch of the tube of unstable IMs from the families of 3-tori LPOs. On the *right* stable IMs from the families D of 2-tori LPOs

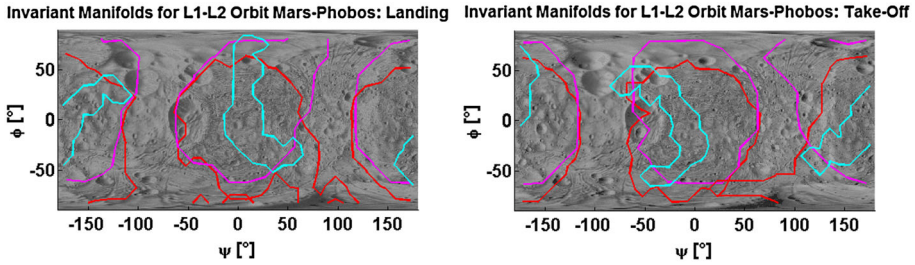

Fig. 25 IMs of the LPOs in the Mars–Phobos ER3BP-GH. On the *left* outer boundaries of the region of the possible landing sites through the IM of all the families of tori around both LPs. On the *right* outer boundaries of the region of the possible take-off sites through the IM of all the families of tori around both LPs. Families' colors are coherent with Fig. 12, with *red* associated to the global family AB

sites is provided in Fig. 25. This area is restricted to the collinear-faced sites on Phobos, due to the collapsing effect of the SOI. In particular, large tori within the families AB and C can extend the region in both longitude and latitude, while the POs and the QPOs of the D branch are more constrained. Also the region of the big crater Stickney is accessible with both stable and unstable IMs of large QPOs of the families AB and C.

We propose using the IMs as natural de-orbiting trajectories that evolve from the LPOs, since they are the asymptotic separatrices of their center manifold. Since the perturbation of the GHs grows exponentially as the proximity to Phobos increases, the globalization of the manifolds, using a low-order series expansion, produces an inaccurate approximation in the final stages of the landing (and first stages of the take-off). This is a common problem for any lander, where the final manoeuvers are managed by the Guidance, Navigation and Control (GNC) subsystem to satisfy the performances required. Results in this section should therefore be considered as an estimation of these performances at the touch-down and launch, more refined than the CR3BP, to lower the load on the GNC subsystem in the real scenario. Focusing on the landing, apart from site and time of flight, the velocity performances at the touch-down considered are: total magnitude, angle of incidence and vertical component. The desired trajectory would minimize the longitudinal control as well as yield a soft landing. In this paper the IM final condition is considered as an input to the final descent undertaken by the GNC subsystem, therefore the aim considered is to minimize the angle of incidence for the

landing. The GNC will then be required to brake the spacecraft horizontally to verticalize the final stages of the descent, starting from a small vertical velocity and so facilitating the shock absorbtion at touch-down. An indicative figure for the shock force could be derived from the law of conservation of momentum, considering an impulse of 0.1 s (inversely proportional to the rigidity of the absorbtion structure): numerically the shock force in terrestrial g is approximately equal to the vertical velocity in m/s. Instead for the take-off the first driver is to minimize the escape velocity (total magnitude).

For an m-parameter family of invariant n-tori, the number of trajectories of the tube of IMs is organized in a (n+m)-dimensional matrix parameterized by the n phases and the m parameters. To exploit the outcomes in the mission design, the performances are reparameterized by the topographical map of the landing/take-off sites, to represent the properties of the optimal trajectory available for each couple of longitude and latitude. Figure 26 presents the velocity performances for the natural landing and take-off opportunities at Phobos. The analysis of these performances shows that highly efficient natural trajectories are able to land tangentially, facilitating a soft controlled touch-down, and depart with a very small escape velocity, less than 30 % of the 2B Δv value, for an extended region of topographical collinear-faced sites on Phobos. These trajectories have the potential to be exploited for future sample-and-return missions to this moon, where free-fall is required to avoid contamination of the sample's soil by the exhaust plume of the thrusters or rockets' nozzle.

5.5 Extension of the LPOs and IMs to model natural impacts on the surface and the dust dynamics around Phobos

The LPOs and IMs presented in this paper have been applied to model the motion of a spacecraft about Phobos. According to our analysis of the orbital perturbations in Sect. 2.2, SRP is not significant if the spacecraft does not use solar sails. SRP becomes important also in the well-known photo-gravitational 3BP for the orbital dynamics of dust grains around the secondary body, because the perturbation a^P is inversely proportional to the grain radius. This is very important for an asteroid, where the SRP could be higher than the Sun 3B perturbation, and affect even a spacecraft. The ratio $a^P/a_\odot$ with the full Solar gravity magnitude $a_\odot$ is known as the lightness number λ. However, an analysis on the order of magnitude of the physical characteristics leads to an interesting outcome for the Mars–Phobos system. The objective here is to study the transition from a classical CR3BP to a photo-gravitational CR3BP. This means to identify the conditions that make the SRP a significant force in the modeling of the dynamics around a body of the Solar System. The transition between the two models is assessed referring λ to the second massive body gravity, which is a^P/a_2. The dust grain is modeled as a sphere, with common physical values (specular and diffusive reflectance coefficients both set to 5 %, and density to 3000 kg/m^3). Thus λ, for a given couple of primaries in the Solar System, is now a function of the grain radius and the distance from the secondary. Assuming a threshold $\lambda = 1\,\%$ to identify when the SRP becomes relevant enough to be included in the modeling of the dynamics, the transition grain radius is computed as a function of the distance from the secondary. This radius does not change order of magnitude inside the SOI of Phobos, due to its small altitude over the body. Its value is quite low: 20 μm at the Hill's radius, and 9 μm on the mean surface. As a difference, if Phobos had been an asteroid orbiting the Sun at the Sun–Mars distance, its gravity field at the LPs would have been 10,000 times smaller, so the equivalent dust grain radius that requires the transition to a photo-gravitational problem would rise to 20 cm.

Therefore, the results obtained in this paper focused on the natural motion around Phobos in the ER3BP-GH, that do not consider the SRP, in addition to common spacecraft, also provide

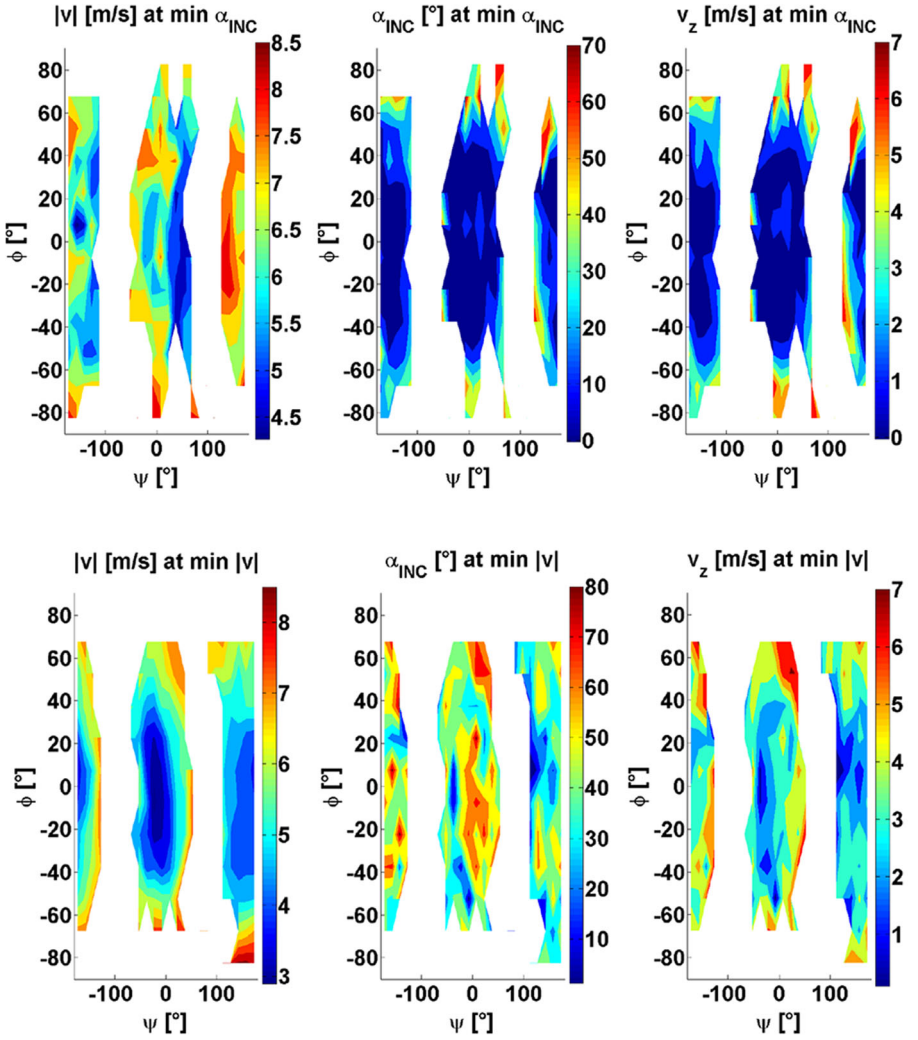

Fig. 26 IMs of the LPOs in the Mars–Phobos ER3BP-GH. On the *top* performances of the trajectories that provide the min incidence at the touch-down from all the families of tori around both LPs, as a function of the longitude and latitude of the landing site on Phobos surface modeled through shape harmonics: velocity magnitude, angle of incidence, downward vertical velocity. On the *bottom* performances of the trajectories that provide the min velocity magnitude at the launch from all the families of tori around both LPs

a good approximation for the natural motion of dust grains down to 10^{-5} m scale. This is a broad range considering the common distribution of minor bodies' regolith (m − 0.01 nm). So for Phobos, only very small dust grains require the photo-gravitational model to be used. This means that the IMs of the ER3BP-GH could be the trajectories followed by a large dimensional range of meteoroids that have impacted Phobos, as well as boulders of regolith that lifted off from its surface, to constitute the orography of its craters distribution. In this sense, Fig. 25 highlights that the medium-small craters are densely accumulated on the two collinear sides where the IMs of the LPOs impact or leave the moon, and their boundaries link neatly together all the larger craters, in particular Stickney and the craters on the Norther

sub-Mars sector. With the help of the map in Fig. 1 of Ramsley and Head III (2013b), it is immediately noticeable that most of the characteristic grooves of Phobos run parallel to the boundary of the regions of landing and take-off sites computed. In particular, recall that only the IMs of the practical LPOs that do not intersect Phobos were considered in this paper, but larger orbits (which refer to higher energy transferred material) provide additional impact trajectories themselves. Their footprint will correspond to the pattern of the remaining grooves, since they both develop farther concentrically on the L_1 and L_2-sides of the moon. Indeed, extending the above calculation for all the major couples of primaries of the Solar System, the two Martian moons have the highest values of transition grain radius on the mean surface among the bodies considered. This means that Phobos and Deimos could experience rings of dust clouds of micrometer scale around them (Krikov et al. 1996) and some authors theorize that dust dynamics on the surface is responsible for the origin of the grooves of Phobos (Ramsley and Head III 2013a, b; Dombard et al. 2010). We suggest that the footprint of IMs and large LPOs could have originated in the past the craters and the grooves of Phobos, and that current dust clouds of grain dimension over 20μm could correspond to the LPOs presented in this paper.

6 Conclusions

The analysis of the natural dynamics inside Phobos' realm of attraction undertaken in this paper has revealed some potential mission opportunities around the Libration points L_1 and L_2. First the classical families of periodic and quasi-periodic Libration Point orbits (LPOs) in the basic CR3BP have been computed for the Mars–Phobos system. The LPOs are well-known exploitable solutions for orbiting about the smaller primary and they provide energy-efficient trajectories for interplanetary transfers of spacecraft through their Invariant Manifolds; however they are highly unstable, and station-keeping is required. For the Mars–Phobos system, the altitude of the Libration points moves very close to Phobos' irregular surface. In this situation, the basic dynamical approximation provided by the CR3BP falls short, and in particular two differential orbital perturbations become relevant in describing the natural relative motion around this moon. They are shown to be its highly inhomogeneous gravity field and its orbital eccentricity.

The dynamical substitutes of the LPOs have been computed in an improved system of the relative dynamics in proximity of Phobos, upgrading the Mars–Phobos ER3BP with the real gravity field of the moon, modeled with a gravity harmonics series expansion. The solutions are derived through numerical continuation techniques that maintain the phase-space of the perturbations. In particular, the effect of the gravity harmonics produces families of periodic and quasi-periodic orbits highly distorted and tilted from the classical case, whereas the effect of the eccentricity causes the orbits to oscillate around these solutions with a significant amplitude for the proximity of Phobos.

Around each collinear side of Phobos, the new LPOs in the ER3BP-GH are constituted by the oscillating Libration points and a 1-parameter family of iso-periodic periodic orbits vertically-elongated with the period of Phobos revolution around Mars, three 1-parameter families of 2-tori quasi-periodic orbits, and two 2-parameter families of 3-tori quasi-periodic orbits. These orbits are very close to the moon's surface, therefore they are similar to close-range points but with an extended ground-track and range of lighting conditions, and the Phobos' bulk occultation of the sky could provide relevant passive shielding from the cosmic rays radiation. Despite their high instability, the LPOs are natural motions and so will require

no propulsion and low station-keeping cost to provide: close-range observation of Phobos, mission segments to directly interface with landing and take-off phases, proximity parking orbits for mothership modules to remotely command lighter probes deployed on the surface, and communication bridges to manage robotic scouts on Mars and Phobos. However, they require the high accuracy of an optical navigation subsystem, and high load on the guidance subsystem, whose reference signal must be computed with advanced analytical and numerical techniques of dynamical systems theory that need the acquisition of a high-fidelity gravity field of the moon. In this sense, in this paper we assessed the accuracies required for the modeling parameters of the ER3BP-GH against the GNC requirements, to track a spacecraft along the reference signal of the new orbits computed in our model. A preliminary estimation proved that such LPOs considerably lower the control load and enhance the fuel savings between one and two orders of magnitude, enabling feasible station-keeping by exploiting the natural dynamics around Phobos.

Another useful application is to exploit the Invariant Manifolds of these new LPOs as landing or take-off gateways to and from the surface of Phobos. In this paper it was proved that there exist natural trajectories for a specific range of longitude-latitude sites able to facilitate a soft controlled landing, and depart with very low escape velocity injections, less than the 2B Δv value. The optimization of these performances to select the best trajectory at a given location on Phobos will be paramount for sample-and-return missions (where soil contamination avoidance is necessary) as well as first manned explorations of this moon.

In addition, the new natural dynamics upgraded with the inhomogeneous gravity field of the moon could provide further evidence to the unique formation of Phobos by Mars' ejecta accretion, and the natural LPOs and Invariant Manifolds could also be related to the craters and grooves distribution's formation of the moon, as well as model the dynamics of the theorized clouds of dust existing on Phobos.

Acknowledgments This work has been supported by the European Commission through the Marie Curie fellowship PITN-GA-2011-289240 "AstroNet-II". We are thankful to Prof. J.J. Masdemont and Prof. G. Gómez (IEEC) for the assistance provided in the computation of LPOs in the CR3BP through high-order series expansions in the early stage of this research.

References

Abouelmagd, E.I., Sharaf, M.A.: The motion around the libration points in the restricted three-body problem with the effect of radiation and oblateness. Astrophys. Space Sci. **344**(2), 321–332 (2013)

Adomaitis, R.A.: The trouble with spurious eigenvalues. Int. J. Bifurc. Chaos **17**(4), 1375–1381 (2007)

Allgower, E.L., Georg, K.: Introduction to numerical continuation methods. In: Classics in Applied Mathematics, vol. 45. Society for Industrial and Applied Mathematics, Philadelphia (2003)

Archinal, B.A., A'Hearn, M.F., Bowell, E., Conrad, A.R., Consolmagno, G.J., Courtin, R., Fukushima, T., Hestroffer, D., Hilton, J.L., Krasinsky, G.A., Neumann, G., Oberst, J., Seidelmann, P.K., Stooke, P., Tholen, D.J., Thomas, P.C., Williams, I.P.: Report of the IAU working group on cartographic coordinates and rotational elements: 2009. Celest. Mech. Dyn. Astron. **109**(2):101–135 (2010). doi:10.1007/s10569-010-9320-4

Arredondo, J.A., Guo, J., Stoica, C., Tamayo, C.: On the restricted three-body problem with oblate primaries. Astrophys. Space Sci. **341**(2), 315–322 (2012)

Baoyin, H., McInnes, C.R.: Trajectories to and from the lagrange points and the primary body surfaces. J. Guid. Control Dyn. **29**(4), 998–1003 (2006)

Bombardelli, C.: Stable artificial equilibrium points in the Mars–Phobos system. In: 1st IAA-AAS conference on dynamics and control of space systems, Porto, March 19–21 (2012)

Brandenburg, J.E.: Mars-Phobos: a Mars mission architecture with Mars-Moon synergy. J. Space Explor. **1**(1):26–33 (2012)

Brannon, R.M.: Curvilinear Analysis in an Euclidian Space. University of New Mexico Supplemental Book Draft. University of New Mexico, Albuquerque (2004)
Broucke, R.: Stability of periodic orbits in the elliptic restricted three-body problem. AIAA J. **7**(6), 1003–1009 (1969)
Campagnola, S., Lo, M., Newton, P.: Subregion of motion and elliptic halo orbits in the elliptic restricted three-body problem. In: 8th AIAA/AAS Space Flight Mechanics Meeting, Glaveston, January 27–31 (2008)
Chao, B.F., Rubincam, D.P.: The gravitational field of Phobos. Geophys. Res. Lett. **16**(8), 859–862 (1989)
Conley, C.C.: Low energy transit orbits in the restricted three-body problem. SIAM J. Appl. Math. **16**, 732–746 (1969)
Craddock, R.A.: Are Phobos and Deimos the result of a giant impact? Icarus **211**(2), 1150–1161 (2011)
da Silva Pais Cabral, F.: On the Stability of Quasi-Satellite Orbits in the Elliptic Restricted Three-Body Problem. Master's thesis, Universidade Técnica de Lisboa (2011)
Dombard, A.J., Barnouin, O.S., Prockter, L.M., Thomas, P.C.: Boulders and ponds on the asteroid 433 Eros. Icarus **210**(2), 713–721 (2010)
Dorminey, B.: Phobos As First Pit Stop in Manned Mars Exploration. http://www.forbes.com/sites/brucedorminey/2013/06/26/phobos-as-potential-first-pit-stop-in-human-mission-to-mars (Online) (2013)
Douskos, C.N., Markellos, V.V.: Out-of-plane equilibrium points in the restricted three-body problem with oblateness. Astron. Astrophys. **446**, 357–360 (2006)
Duxbury, T.C., Callahan, J.D.: Pole and prime meridian expressions for Phobos and Deimos. Astron. J. **86**(11), 1722–1727 (1981)
Farquhar, R.W.: The Control and Use of Libration-Point Satellite. PhD thesis, Stanford University (1968)
Genta, G., Dupas, A., Salotti, J.M.: IAA study group on global human Mars system missions exploration. In: 65th International Astronautical Congress, Toronto, September 29-October 3 (2014)
Gil, P.J.S.: QSO: Current state of the art and mission analysis results for a class of Phobos observation and access orbits. In: 3rd International Workshop on Spaceflight Dynamics and Control, Covilhã, October 9 (2007)
Gil, P.J.S., Schwartz, J.: Simulations of quasi-satellite orbits around Phobos. J. Guid. Control Dyn. **33**(3), 901–914 (2010)
Gómez, G., Mondelo, J.M.: The dynamics around the collinear equilibrium points of the restricted three-body problem. Physica D **157**(4), 283–321 (2001)
Gómez, G., Jorba, A., Masdemont, J. J., Simó, C.: Study Refinement of Semi-analytical Halo Orbit Theory. Final report ESOC contract (1991)
Gómez, G., Masdemont, J.J., Mondelo, J.M.: The dynamical substitutes of the libration points for simplified solar system models. In: Libration Point Orbits and Applications, Aiguablava, June 10–14 (2002)
Hopkins, J.B., Pratt, W.D.: Comparison of Deimos and Phobos as destinations for human exploration, and identification of preferred landing sites. In: AIAA Space 2011 Conference & Exposition, Long Beach, September 27–29 (2011)
Hou, X.Y., Liu, L.: On motions around the collinear libration points in the elliptic restricted three-body problem. Mon. Not. R. Astron. Soc. **415**, 3552–3560 (2011)
Howell, K.C.: Three-dimensional, periodic, 'Halo' orbits. Celest. Mech. **32**(53), 53–71 (1984)
Jorba, A.: Numerical computation of the normal behavior of invariant curves of n-dimensional maps. Nonlinearity **14**, 943–976 (2001)
Kaula, W.M.: Theory of Satellite Geodesy. Blaisdell, Waltham (1966)
Keller, H.B.: Numerical Solution of Bifurcation and Nonlinear Eigenvalue Problems. Applications of Bifurcation Theory. Academic Press, New York City (1977)
Kolemen, E., Kasdin, N.J., Gurfil, P.: Multiple Poincaré sections method for finding the quasiperiodic orbits of the restricted three-body problem. Celest. Mech. Dyn. Astron **112**, 47–74 (2012)
Koon, W.S., Lo, M.W., Marsden, J.E., Ross, S.D.: Heteroclinic connections between periodic orbits and resonance transitions in celestial mechanics. Chaos **10**, 427–469 (2000)
Koon, W.S., Lo, M.W., Marsden, J.E., Ross, S.D.: Dynamical Systems, The Three-Body Problem and Space Mission Design. Springer, New York City (2011)
Koschny, D.: Phootprint: An ESA mission study. In: Mars Concepts and Approaches Workshop, Houston, June 12–14 (2012)
Krikov, A.V., Sokolov, L.L., Dikarev, V.V.: Dynamics of Mars-orbiting dust: effects of light pressure and planetary oblateness. Celest. Mech. Dyn. Astron. **63**, 313–339 (1996)
Lee, P.: Phobos and Deimos update. In: 7th SBAG Meeting, Pasadena, July 10–11 (2012)
Lidov, M.L., Vashkov'yak, M.A.: Theory of perturbations and analysis of the evolution of quasi-satellite orbits in the restricted three-body problem. Cosm. Res. **31**, 75–99 (1993)

Martinec, Z., Pěč, K., Burša, M.: The Phobos gravitational field modeled on the basis of its topography. Earth Moon Planets **45**, 219–235 (1989)
Masdemont, J.J.: High order expansions of invariant manifolds of libration point orbits with applications to mission design. Dynamical Systems: An International Journal **20**(1), 59–113 (2004)
Masdemont, J.J., Mondelo, J.M.: Notes for the numerical and analytical techniques lectures. In: Advanced Topics in Astrodynamics Summer Course, Institut d'Estudis Espacials de Catalunya, Barcelona (2004)
McCaughrean, M.: ESA's Report to the 39th COSPAR Meeting. ESA Communications, Noordwijck (2012)
McGehee, R.: Some Homoclinic Orbits for the Restricted Three-Body Problem. PhD thesis, University of Wisconsin (1969)
Ni, Y., Baoyin, H., Li, J.: Orbit dynamics in the vicinity of asteroids with solar perturbation. In: 65th International Astronautical Congress, Toronto, September 29-October 3 (2014)
O'Leary, B.: Rationales for early human missions to Phobos and Deimos. In: Mendell, W.W. (ed.) Lunar Bases and Space Activities of the 21st Century, pp. 801–808. Lunar and Planetary Institute, Houston (1985)
Olikara, Z., Scheeres, D.J.: Numerical methods for computing quasi-periodic orbits and their stability in the restricted three-body problem. In: 1st IAA-AAS Conference on Dynamics and Control of Space Systems, Porto, March 19–21 (2012)
Pandika, M.: Stanford Researchers Develop Acrobatic Space Rovers to Explore Moons and Asteroids. http://news.stanford.edu/news/2012/december/rover-mars-phobos-122812.html, [Online] (2012)
Price, H.W., Woolley, R.C., Strange, N.J., Baker, J.D.: Human missions to Mars orbit, Phobos, and Mars surface using 100-kWe-class solar electric propulsion. In: AIAA Space 2014 Conference, San Diego, August 4–7 (2014)
Ramsley, K.R., Head III, J.W.: Mars imapct ejecta in the regolith of Phobos: bulk concentration and distribution. Planet. Space Sci. **87**, 115–129 (2013a)
Ramsley, K.R., Head III, J.W.: The origin of Phobos grooves from ejecta launched from impact craters on Mars: test of the hypothesis. Planet. Space Sci. **75**, 69–95 (2013b)
Richardson, D.L.: Analytic construction of periodic orbits about the collinear points. Celest. Mech. **22**, 241–253 (1980)
Rosenblatt, P.: The origin of the Martian moons revisited. Astron. Astrophys. Rev. **19**(1):44 (2011)
Rosenblatt, P., Charnoz, C.: On the formation of the Martian moons from a circum-mars accretion disk. In: 46th ESA ESLAB Symposium: Formation and Evolution of Moons, Noordwijk, June 25–28 (2012)
Singer, S.F.: The PhD proposal: A manned mission to Phobos and Deimos. In: The case for Mars Conference, Boulder, April 29–May 2 (1981)
Sommerer, J.: Technical and programmatic prospects for human space exploration 2015–2030. In: 65th International Astronautical Congress, Toronto, Sept 29–Oct 3 (2014)
Stoer, J., Bulirsch, R.: Introduction to Numerical Analysis. Springer, New York City (1983)
Szebehely, V.: Theory of Orbits: The Restricted Problem of Three Bodies. Academic Press, New York City (1967)
Troutman, P.: The evolvable Mars campaign: the moons of Mars as a destination. In: 11th NASA Small Body Assessment Group Meeting, Washington, July 29–31 (2014)
Turner, R.J.: A model of Phobos. Icarus **33**, 116–140 (1978)
Wallace, M.S., Parker, J.S., Strange, N.J., Grebow, D.: Orbital operations for Phobos and Deimos exploration. In: AIAA-AAS Astrodynamics Specialist Conference, Minneapolis, Aug 13–16 (2012)
Werner, R.A.: The gravitational potential of a homogeneous polyhedron or don't cut corners. Celest. Mech. Dyn. Astron. **59**, 253–278 (1994)
Willner, K.: The Martian Moon Phobos. A Geodetic Analysis of Its Motion, Orientation, Shape, and Physical Parameters. PhD thesis, Technische Universität Berlin (2009)
Yu, Y., Baoyin, H.: Generating families of 3D periodic orbits about asteroids. Mon. Not. R. Astron. Soc. **427**, 872–881 (2012a)
Yu, Y., Baoyin, H.: Orbital dynamics in the vicinity of asteroid 216 Kleopatra. Astron. J. **143**(3), 62–70 (2012b)